Including directly measured rotations in the virtual point transformation

Tomaž Bregar[a], Nikola Holeček[a], Gregor Čepon[b,*], Daniel J. Rixen[c], Miha Boltežar[b]

[a] *Gorenje d.d., Partizanska 12, 3503 Velenje, Slovenia*
[b] *Faculty of Mechanical Engineering, University of Ljubljana, Aškerčeva 6, 1000 Ljubljana, Slovenia*
[c] *Technische Universität München, Institute for Applied Mechanics, Boltzmannstr. 15, 85748 Garching, Germany*

Abstract

Dynamic substructuring methods serve as a powerful tool in the analysis of modern complex systems. The coupling of substructures has been successful with analytically obtained results. However, substructuring with experimentally obtained data remains challenging. One of the main problems associated with experimental substructuring is the coupling of the rotational degrees of freedom (RDoFs). A promising method where RDoFs are included implicitly is the virtual point transformation. Even though the transformation has been successfully used in the substructuring process, it is still highly susceptible to inaccuracies in the sensor sensitivity and positioning. In this paper an expansion to the virtual point transformation is proposed, which enables the projection of a directly measured rotation response on the interface deformation modes. A novel formulation of the weighting matrix is introduced to consistently include the measured rotations in the transformation. The proposed expansion is demonstrated on a numerical model of a simple beam-like structure and compared with the standard transformation. The effects of inaccuracies in the sensor sensitivity and placement on the overall quality of both transformation are analysed with a global sensitivity analysis. Finally, an experimental validation of the proposed expansion is carried out on a steel beam.

*Corresponding author
Email address: `gregor.cepon@fs.uni-lj.si` (Gregor Čepon)

Keywords: Frequency Based Substructuring, Virtual Point Transformation, Interface Rotation, Rotational Degrees of Freedom, Global Sensitivity analysis

1. Introduction

Dynamic substructuring (DS) enables us to assemble the dynamic properties of subsystems and accordingly predict the dynamic response of a complete system. Evaluating the subsystem dynamics separately can be advantageous, since each subsystem can either be developed by a different design team or it would be beneficial to evaluate and optimise the design separately, due to the geometrical complexity of the subsystem. The formulation for DS methods is well defined [1, 2] and coupling with analytical or numerical data is consistent. However, coupling with experimentally obtained data has proven to be problematic [3, 4, 5]. For this reason, methods to improve the experimental dynamic substructuring are still the subject of ongoing research.

One of the DS methods is known as frequency-based substructuring (FBS), which is based on a response model and was first published by Jetmundsen et al. [6]. The FBS is also known as Admittance modeling [7, 8] or Impedance coupling [9]. The method was reformulated in 2006 by de Klerk et al. [10] to the Lagrange Multiplier FBS method (LM FBS). The main challenge in LM FBS coupling is the interface modelling and obtaining a full-degrees-of-freedom (DoFs) frequency-response-functions (FRFs) matrix with translational and also rotational DoFs. Coupling substructures without rotational DoFs can lead to erroneous results [11, 12, 13]. Generating rotational FRFs from a numerical model is straightforward; however, an experimental measurement of the rotational response is still problematic. Therefore, various methods were developed to implicitly account for rotational DoFs. The system equivalent reduction and expansion (SEREP) procedure [14] was used to include rotational DoFs in coupling by Williams et al. [15]. Rotational mode shapes were deduced by measuring the strain by Kim et al. [16]. Precisely positioned translation accelerometers were used to obtain the rotational response with the finite-differences theory [17, 18]. Silva et al. [19] estimated the rotational response based on a modified Kidder's method. A full 6×6 receptance matrix was measured using an X-block attachment in two different positions by Mottershead et al. [20] for the structural modification of a helicopter tailcone. Mayes et al. [21, 22] proposed a transmission simulator concept to couple the continuous interface based on modal constraints for fixtures and subsystems (MCFS) [23].

Additionally, for the LM FBS formulation the interface DoFs must be collocated on both substructures, which in practice is often hard to achieve. A method that solves the inclusion of rotational DoFs and the collocation of the interface DoFs for a discrete interface is the so-called virtual point transformation (VPT) [24]. The VPT is an upgrade of the equivalent multiple point connection (EMPC) [25] method. Transformation projects measured the translational DoFs on so-called interface deformation modes (IDMs), which are assumed to describe the dynamics of the interface. The interface can be modelled as rigid or extended with a flexible interface mode as shown in [5]. The whole transformation can also be interpreted as a minimization procedure [26].

The objective of this paper is to present an expansion of the virtual point transformation with measured rotational responses. A combined transformation matrix is derived, which enables the projection of a directly measured rotational response on the interface deformation modes. It is shown in [27] that direct rotational sensors are less prone to errors in measuring rotations than indirect methods. In addition, a direct quartz-based piezoelectric rotational accelerometer was successfully used by Drozg et al. [11] to obtain a full DoFs FRF matrix. In order to present the capability of the extension proposed in this paper, standard and expanded virtual point transformations were applied on a numerical model of a simple beam-like structure and evaluated. Additionally, two separate global sensitivity analyses were performed to examine the effect of small deviations in the sensor placement and sensitivity on the overall quality of both transformations. Furthermore, the proposed expansion was experimentally validated on a steel beam.

The paper is organized as follows. The next section briefly summarizes the LM FBS method and the virtual point transformation. The third section presents an expansion where directly measured rotational degrees of freedom are introduced to the virtual point transformation. The fourth section presents a numerical case study on a simple beam-like structure, where the effect of uncertainty in the sensor location and sensor sensitivity on the overall quality of both transformations was analysed with a global sensitivity analysis. In the fifth section the practical applicability of the proposed expansion is demonstrated. In the last section a summary and the contributions are presented.

2. Virtual point transformation

This section introduces the basic theory of the virtual point transformation, starting with a recap of the LM FBS method [10]. With frequency-based substructuring (FBS) we can determine the admittance of the assembled system $\mathbf{Y}^{AB}$ from the separate admittances of two substructures $\mathbf{Y}^{A}$ and $\mathbf{Y}^{B}$ (Fig. 1). The governing equation of motion for two uncoupled substructures

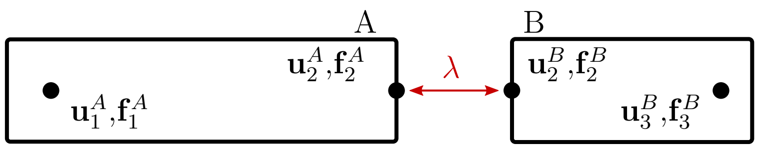

Figure 1: Schematic representation of the substructuring problem.

is equal to:[1]

$$\mathbf{Y}^{A|B}(\mathbf{f}+\mathbf{g}) = \begin{bmatrix} \mathbf{Y}_{11}^{A} & \mathbf{Y}_{12}^{A} & 0 & 0 \\ \mathbf{Y}_{21}^{A} & \mathbf{Y}_{22}^{A} & 0 & 0 \\ 0 & 0 & \mathbf{Y}_{22}^{B} & \mathbf{Y}_{23}^{B} \\ 0 & 0 & \mathbf{Y}_{32}^{B} & \mathbf{Y}_{33}^{B} \end{bmatrix} \left(\begin{bmatrix} \mathbf{f}_1^A \\ \mathbf{f}_2^A \\ \mathbf{f}_2^B \\ \mathbf{f}_3^B \end{bmatrix} + \begin{bmatrix} 0 \\ \mathbf{g}_2^A \\ \mathbf{g}_2^B \\ 0 \end{bmatrix} \right) = \begin{bmatrix} \mathbf{u}_1^A \\ \mathbf{u}_2^A \\ \mathbf{u}_2^B \\ \mathbf{u}_3^B \end{bmatrix} = \mathbf{u}, \quad (1)$$

where $\mathbf{u}$ denotes the displacements, $\mathbf{f}$ is the vector of external forces and $\mathbf{g}$ is the vector of interface forces between the two substructures in the coupled state. To couple the substructures we need to define a connection between the two. A signed Boolean matrix $\mathbf{B}$ enforces the conditions of compatibility:

$$\mathbf{B}\mathbf{u} = 0, \quad (2)$$

and also the conditions of equilibrium:

$$\mathbf{g} = -\mathbf{B}^{\mathrm{T}}\boldsymbol{\lambda}, \quad (3)$$

where $\boldsymbol{\lambda}$ are Lagrange multipliers representing reaction forces. Inserting Eq. (2) and Eq. (3) into Eq. (1) and eliminating $\boldsymbol{\lambda}$ yields the admittance matrix of the assembled system:

$$\mathbf{Y}^{AB}\mathbf{f} = \left(\mathbf{Y}^{A|B} - \mathbf{Y}^{A|B}\mathbf{B}^{\mathrm{T}}\left(\mathbf{B}\mathbf{Y}^{A|B}\mathbf{B}^{\mathrm{T}}\right)^{-1}\mathbf{B}\mathbf{Y}^{A|B}\right)\mathbf{f} = \mathbf{u}. \quad (4)$$

[1] An explicit dependency on frequency is omitted for simplicity of the notation, as will be done for the remainder of the paper.

The LM FBS method is based on a full-DOF response model, with collocated interface degrees of freedom (DoFs). In practice, it is often the case that neither the sensors nor the excitation points are in the same positions for the two substructures; therefore, the two substructures cannot be directly coupled with the LM FBS method.

A virtual point transformation (VPT) enables us to couple two substructures with non-collocated interface DoFs. The theory of the VPT in this section summarizes the work of M. V. van der Seijs et al. [24, 2]. The main idea behind the VPT is to choose a virtual point near the physical interface of the substructures and project the measured sensor displacements and force inputs onto the interface deformation modes (IDMs). If we assume only the rigid-body IDMs then we have $m = 6$ DoFs for each virtual point (3 translations and 3 rotations). In addition, flexible deformation modes can also be added to model more complex connections [5]. The actual transformation is achieved with the following equation:

$$\mathbf{Y}_{\mathrm{qm}} = \mathbf{T}_{\mathrm{u}} \mathbf{Y}_{22} \mathbf{T}_{\mathrm{f}}^{\mathrm{T}}, \tag{5}$$

where $\mathbf{Y}_{22}$ denotes the admittance FRF of the non-collocated interface DoFs (i.e., $\mathbf{u}_2^A$ and $\mathbf{u}_2^B$), $\mathbf{T}_{\mathrm{u}}$ is the displacement transformation matrix derived in Section 2.1 and $\mathbf{T}_{\mathrm{f}}$ is the force transformation matrix derived in Section 2.2. $\mathbf{Y}_{\mathrm{qm}}$ is the VP FRF matrix with a perfectly collocated force and displacement DoF. With the resulting VP FRF matrix, the substructures can be coupled with the LM FBS method.

2.1. Interface displacement reduction

Interface displacement reduction is achieved with a set of interface displacement modes (IDMs) contained in the matrix $\mathbf{R}_{\mathrm{u}} \in \mathbb{R}^{n_{\mathrm{u}} \times m}$. We want to express n_{u} measured interface displacements with m IDMs. A simple interface connection is depicted in Fig. 2. If we consider only the rigid IDMs then the VP has 6 DoFs. That is three translations $q_{\mathrm{t}}^{\nu} = [q_X^{\nu}, q_Y^{\nu}, q_Z^{\nu}]$, where the superscript ν refers to a specific VP of a substructure, and three rotations $q_{\theta}^{\nu} = [q_{\theta_X}^{\nu}, q_{\theta_Y}^{\nu}, q_{\theta_Z}^{\nu}]$. The following kinematic relation can be written between the virtual point DoF $\mathbf{q}^{\nu}$ and the sensor displacement $\mathbf{u}^k$, provided that we

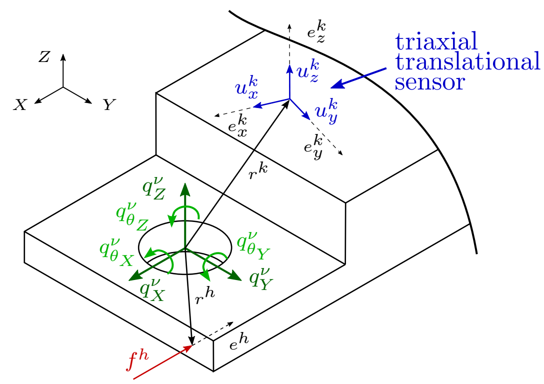

Figure 2: Interface connection example with virtual point and triaxial translation sensor.

know the sensor location and orientation:

$$\begin{bmatrix} u_x^k \\ u_y^k \\ u_z^k \end{bmatrix} = \begin{bmatrix} e_{x,X}^k & e_{x,Y}^k & e_{x,Z}^k \\ e_{y,X}^k & e_{y,Y}^k & e_{y,Z}^k \\ e_{z,X}^k & e_{z,Y}^k & e_{z,Z}^k \end{bmatrix} \begin{bmatrix} 1 & 0 & 0 & 0 & r_Z^k & -r_Y^k \\ 0 & 1 & 0 & -r_Z^k & 0 & r_X^k \\ 0 & 0 & 1 & r_Y^k & -r_X^k & 0 \end{bmatrix} \begin{bmatrix} q_X^\nu \\ q_Y^\nu \\ q_Z^\nu \\ q_{\theta_X}^\nu \\ q_{\theta_Y}^\nu \\ q_{\theta_Z}^\nu \end{bmatrix} + \begin{bmatrix} \mu_{u_x}^k \\ \mu_{u_y}^k \\ \mu_{u_z}^k \end{bmatrix}, \tag{6}$$

where $[e_{x,X}^k, e_{y,X}^k, e_{Z,X}^k]^\mathrm{T}$ are the coordinates of the unit direction X of sensor k represented in the global reference frame of the structure and the vector $\boldsymbol{\mu}_\mathrm{u}^k$ contains any residual motion, not included in the subspace of IDMs. If the rigid assumption of the interface is valid in the considered frequency range, then the residual motion in $\boldsymbol{\mu}_\mathrm{u}^k$ will most likely be negligible. Eq. (6) can be expanded to include all the measured displacements:

$$\mathbf{u} = \mathbf{R}_\mathrm{u}\mathbf{q} + \boldsymbol{\mu}_\mathrm{u}. \tag{7}$$

A symmetrical weighting matrix $\mathbf{W}_\mathrm{u}$ is introduced to gain more control over the transformation and the equation is solved in a least-mean-square sense (minimizing the $\mathbf{W}_\mathrm{u}$-norm of the residual) for $\mathbf{q}$:

$$\mathbf{q} = (\mathbf{R}_\mathrm{u}^\mathrm{T}\mathbf{W}_\mathrm{u}\mathbf{R}_\mathrm{u})^{-1}\mathbf{R}_\mathrm{u}^\mathrm{T}\mathbf{W}_\mathrm{u}\mathbf{u}. \tag{8}$$

The residual displacement is then equal to:

$$\mathbf{R}_\mathrm{u}^\mathrm{T}\mathbf{W}_\mathrm{u}\boldsymbol{\mu}_\mathrm{u} = 0. \tag{9}$$

Eq. (8) can be further simplified and the displacement transformation matrix $\mathbf{T}_\mathrm{u}$ is defined as:

$$\mathbf{q} = \mathbf{T}_\mathrm{u}\mathbf{u} \qquad \text{where} \qquad \mathbf{T}_\mathrm{u} \triangleq (\mathbf{R}_\mathrm{u}^\mathrm{T}\mathbf{W}_\mathrm{u}\mathbf{R}_\mathrm{u})^{-1}\mathbf{R}_\mathrm{u}^\mathrm{T}\mathbf{W}_\mathrm{u}. \tag{10}$$

2.2. Interface force reduction

For the interface force reduction a similar matrix containing IDMs is constructed. From the interface example in Fig. 2 it is clear that the force f^h will result in a virtual point load $\mathbf{m}^\nu$. Therefore, the following relation can be written:

$$\begin{bmatrix} m_X^\nu \\ m_Y^\nu \\ m_Z^\nu \\ m_{\theta_X}^\nu \\ m_{\theta_Y}^\nu \\ m_{\theta_Z}^\nu \end{bmatrix} = \begin{bmatrix} 1 & 0 & 0 \\ 0 & 1 & 0 \\ 0 & 0 & 1 \\ 0 & -r_Z^h & r_Y^h \\ r_Z^h & 0 & -r_X^h \\ -r_Y^h & r_X^h & 0 \end{bmatrix} \begin{bmatrix} e_X^h \\ e_Y^h \\ e_Z^h \end{bmatrix} f^h. \tag{11}$$

The contribution from the n_f input forces can be combined and accordingly Eq. (11) can be expanded as follows:

$$\mathbf{m} = \mathbf{R}_\mathrm{f}^\mathrm{T}\mathbf{f}, \tag{12}$$

where $\mathbf{R}_\mathrm{f}^\mathrm{T} \in \mathbb{R}^{m \times n_\mathrm{f}}$ is the matrix containing IDMs. In order to perform the virtual point transformation according to Eq. (5), a force transformation matrix $\mathbf{T}_\mathrm{f}^\mathrm{T}$ is needed. Eq. (12) is typically under-determined since $n_\mathrm{f} \geq m$; therefore, inversion is achieved with the weighted right inverse of $\mathbf{R}_\mathrm{f}^\mathrm{T}$ (i.e. finding a solution that has a minimal $\mathbf{W}_\mathrm{f}-$norm):

$$\tilde{\mathbf{f}} = \mathbf{W}_\mathrm{f}\mathbf{R}_\mathrm{f}(\mathbf{R}_\mathrm{f}^\mathrm{T}\mathbf{W}_\mathrm{f}\mathbf{R}_\mathrm{f})^{-1}\mathbf{m}, \tag{13}$$

where $\mathbf{W}_\mathrm{f}$ is a symmetrical weighting matrix. Eq. (13) can be further rewritten:

$$\tilde{\mathbf{f}} = \mathbf{T}_\mathrm{f}^\mathrm{T}\mathbf{m} \qquad \text{where} \qquad \mathbf{T}_\mathrm{f}^\mathrm{T} \triangleq \mathbf{W}_\mathrm{f}\mathbf{R}_\mathrm{f}(\mathbf{R}_\mathrm{f}^\mathrm{T}\mathbf{W}_\mathrm{f}\mathbf{R}_\mathrm{f})^{-1}. \tag{14}$$

If we were to choose sensor faces for the impact locations the absolute values in the matrices $\mathbf{R}_\mathrm{u}$ and $\mathbf{R}_\mathrm{f}$ would be the same [28, 29]. However, the obtained FRFs would exhibit poor coherence; therefore, the use of sensor faces as impact locations is discouraged [2].

Appropriate position of sensors and impact locations is necessary for obtaining a consistent virtual point transformation. The sensors and impact locations should be in the proximity of the VP to avoid the local deformation around the VP. However, with decreased distance the uncertainties associated with the position and orientation are increased. Therefore, the response and excitation positions should be evaluated after the VPT with the measurement-quality indicators [2].

3. A VPT with a rotational response

Rotational DoFs are essential for a successful coupling of two substructures. The standard VPT enables us to indirectly measure and include the RDoFs in substructuring. The reconstruction of the rotational response for the VPT follows a similar methodology as the reconstruction from two precisely positioned translational accelerometers attached on a T-element, as proposed by Ewins et al. [30]. In practice the rotational response obtained from indirect methods often displays poor overall quality [27]. One of the reasons is the fact that the output signal from the translation movement tends to overshadow the signal from the rotational motion [31]. This makes indirect methods liable to inaccuracies in the sensor positions and the sensitivity mismatch [32].

In order to demonstrate the influence of small deviations in the sensor sensitivity, a simple numerical simulation of a cantilever beam is performed, as depicted in Fig. 3. Two translation sensors are placed on the free end of the beam. From the two translations u_1 and u_2, the rotation θ is determined with finite differences. In Fig. 4a the translational FRF with and without a 5% calibration inaccuracy are shown.[2] As expected, only a small difference can be seen between the two. However, the same error in the sensitivity leads to an erroneous rotational FRF, as shown in Fig. 4b. The uncertainties associated with the accelerometer sensitivity are determined by the sensor quality and the calibration procedure. According to ISO 16063-21 [33] the expanded uncertainty for sensitivity can be up to 10% for a calibration in comparison to a reference accelerometer.

[2]Deviation in the sensor sensitivity was simulated as a constant additive noise throughout the whole frequency range ($Y_{\mathrm{u}_2}^{\mathrm{err}} = (1 + s_e) Y_{\mathrm{u}_2}$), where s_e is the percentage calibration error.

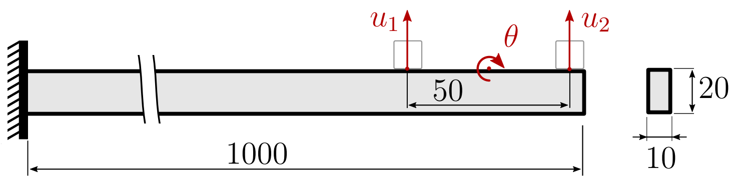

Figure 3: Schematic representation of a cantilever beam with two translation sensors placed on the free end.

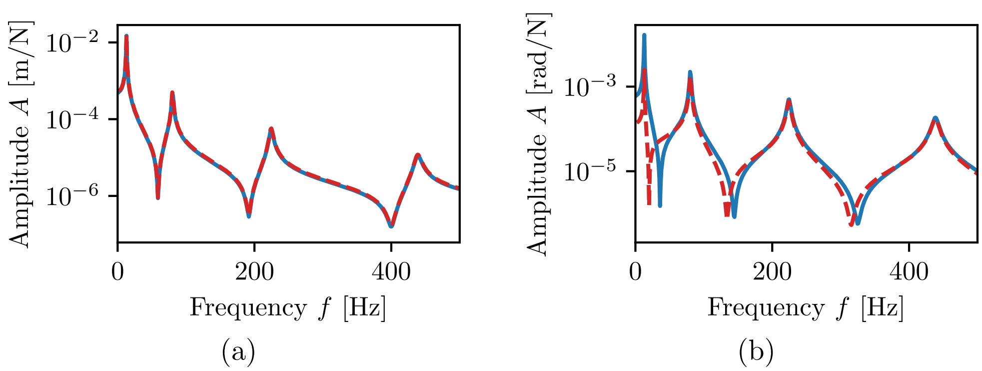

Figure 4: Effect of calibration error in the sensor sensitivity: a) translational FRF Y_{u_2}; b) rotational FRF Y_{θ}. Without calibration error (—), 5% calibration error (- - -).

In a similar way, inaccuracies associated with the sensor sensitivity and the position can influence the quality of the VPT. However, with the VPT the number of measured DoFs is usually larger than the number of IDMs. Consequently, the transformation is overdetermined and the errors on a single sensor are reduced due to the least-squares fit. Nonetheless, small inaccuracies in the sensor sensitivity and the sensor location are still significant.

The disadvantages of indirect methods lead to the development of a direct, quartz-based, piezoelectric, rotational accelerometer [34]. To expand the VPT with the incorporation of the directly measured rotational response, in this paper a triaxial rotation sensor on a simple interface is considered, as depicted in Fig. 5.

The main idea behind the transformation stays the same: the measured rotational response is projected onto the interface deformation modes to obtain the collocated VP FRF Matrix. The following kinematic relation can

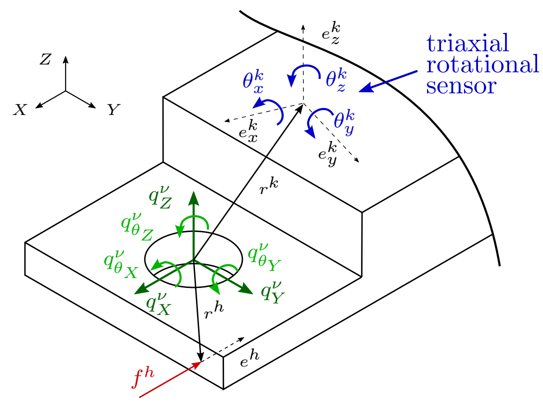

Figure 5: Interface example with virtual point and triaxial rotational sensor.

be written between the virtual point DoF $\mathbf{q}^\nu$ and the sensor rotation $\boldsymbol{\theta}^k$:

$$\begin{bmatrix}\theta_x^k\\ \theta_y^k\\ \theta_z^k\end{bmatrix} = \begin{bmatrix} e_{x,X}^k & e_{x,Y}^k & e_{x,Z}^k \\ e_{y,X}^k & e_{y,Y}^k & e_{y,Z}^k \\ e_{z,X}^k & e_{z,Y}^k & e_{z,Z}^k \end{bmatrix} \begin{bmatrix} 0&0&0&1&0&0\\ 0&0&0&0&1&0\\ 0&0&0&0&0&1 \end{bmatrix} \begin{bmatrix} q_X^\nu \\ q_Y^\nu \\ q_Z^\nu \\ q_{\theta_X}^\nu \\ q_{\theta_Y}^\nu \\ q_{\theta_Z}^\nu \end{bmatrix} + \begin{bmatrix}\mu_{\theta_x}^k\\ \mu_{\theta_y}^k\\ \mu_{\theta_z}^k\end{bmatrix}, \tag{15}$$

where $\boldsymbol{\mu}_\theta^k$ contains any residual motion. The same as for the translational response applies here: if the rigid assumption is valid the residual motion is negligible. If Eq. (6) is compared with Eq. (15) the advantages of the proposed expansion are clear. The kinematic relation for the rotations is dependent only on the sensor orientation, whereas with translations the relation is dependent on the sensor orientation and also the sensor position. Eq. (15) can be expanded to include all the directly measured rotations:

$$\boldsymbol{\theta} = \mathbf{R}_\theta \mathbf{q} + \boldsymbol{\mu}_\theta. \tag{16}$$

Eq. (7) and Eq. (16) can be combined for all the measured displacements and rotations as follows:

$$\begin{bmatrix}\boldsymbol{u}\\ \boldsymbol{\theta}\end{bmatrix} = \begin{bmatrix}\mathbf{R}_\mathrm{u}\\ \mathbf{R}_\theta\end{bmatrix}\mathbf{q} + \begin{bmatrix}\boldsymbol{\mu}_\mathrm{u}\\ \boldsymbol{\mu}_\theta\end{bmatrix} = \mathbf{R}_{\mathrm{u},\theta}\mathbf{q} + \boldsymbol{\mu}_{\mathrm{u},\theta}. \tag{17}$$

To solve Eq. (17) for $\mathbf{q}$ in a minimal-quadratic sense, the norm of the weighted residuals on the displacements and rotations is minimized:

$$\mathbf{q} = \operatorname{argmin}\left(\begin{bmatrix}\boldsymbol{\mu}_{\mathrm{u}} \\ \boldsymbol{\mu}_{\theta}\end{bmatrix}^{\mathrm{T}} \mathbf{W}_{\mathrm{u},\theta} \begin{bmatrix}\boldsymbol{\mu}_{\mathrm{u}} \\ \boldsymbol{\mu}_{\theta}\end{bmatrix}\right) \quad \text{where} \quad \mathbf{W}_{\mathrm{u},\theta} = \operatorname{diag}\big[\mathbf{W}_{\mathrm{u}}, \mathbf{W}_{\theta}\big]. \tag{18}$$

In this approach, the rotations of the VP are not determined solely by the rotational DoFs. Indeed, the VP rotations also influence the translation residual (see Eq. (6)), and the degrees of freedom computed by Eq. (18) for the VP minimize $\boldsymbol{\mu}_{\mathrm{u}}^{\mathrm{T}}\mathbf{W}_{\mathrm{u}}\boldsymbol{\mu}_{\mathrm{u}} + \boldsymbol{\mu}_{\theta}^{\mathrm{T}}\mathbf{W}_{\theta}\boldsymbol{\mu}_{\theta}$. Therefore, rotational DoFs can still be estimated even if less than 3 rotations are directly measured for a VP.

As explained above, the Eq. (18) minimizes the sum of residual on the translation and rotational sensors. Therefore, in order to evaluate both residuals in a comparable norm, a proper weighting matrix for the rotations should be used.

Consider that the rotational measurement around x axis at rotation sensor k has a residual $\mu_{\theta_x}^{k}$ (see Fig. 5). If the VP would be given that residual rotation, the sensor would undergo a displacement $\mu_{\theta_x}^{k} I_x^k$, where I_x^k is the distance between the x axis across the VP and the sensor location and is equal to $\sqrt{r_y^2 + r_z^2}$. A similar reasoning can be done for the rotational residuals around the other axes and for each additional rotational sensor. If the norm of overall displacements due to the rotational residuals at the VP is chosen to be minimised, the following rotational weighting matrix should be used:

$$\mathbf{W}_{\theta} = \operatorname{diag}\Big[\big(I_x^k\big)^2, \big(I_y^k\big)^2, \big(I_z^k\big)^2, \dots\Big]. \tag{19}$$

With the proposed formulation of the rotational weighting matrix the Eq. (17) can be solved for $\mathbf{q}$ and the combined transformation matrix $\mathbf{T}_{\mathrm{u},\theta}$ is obtained:

$$\mathbf{q} = \mathbf{T}_{\mathrm{u},\theta} \begin{bmatrix}\boldsymbol{u} \\ \boldsymbol{\theta}\end{bmatrix} \qquad \text{where} \qquad \mathbf{T}_{\mathrm{u},\theta} \triangleq (\mathbf{R}_{\mathrm{u},\theta}^{\mathrm{T}}\mathbf{W}_{\mathrm{u},\theta}\mathbf{R}_{\mathrm{u},\theta})^{-1}\mathbf{R}_{\mathrm{u},\theta}^{\mathrm{T}}\mathbf{W}_{\mathrm{u},\theta}. \tag{20}$$

The proposed formulation of the combined weighting matrix is minimizing the norm of the displacement residuals for each translation sensor, and for each rotational sensor the norm of overall displacement due to the rotational residual at the virtual point. Therefore, the residuals from the rotational and translation sensors can be compared and Eq. (18) is consistent (assuming $\mathbf{W}_{\mathrm{u}}$ is taken as identity).

Note that the positions of the rotational sensors are only used to define a proper norm for the least square problem: if the rotational measurements were all perfect, the rotation of the VP would be found exactly, notwithstanding any error in the position of those sensors (see Eq. (15)). This is not the case when rotations are derived from the translation sensors (see Eq. (6)). A specific case for the proposed weighting matrix is when the rotations would be measured right at the VP. Then the weighting matrix $\mathbf{W}_\theta$ (Eq. (19)) would become a zero matrix and the directly measured rotational response would be excluded from the transformation. Therefore, the expanded VPT cannot be used when the rotations are measured perfectly at the VP. However, the position of the VP can always be moved away from the position of the rotational accelerometer, since the position of the VP in the vicinity of the interface is arbitrary to some extent. This limit case shows however that the scaling proposed, based on pure geometrical reasoning, is probably not the ultimate choice and maybe different scaling strategies should be developed in the future.

3.1. Measurement-quality indicators

One of the most important features of the virtual point transformation is also the capability to assess the overall quality of the measurement. Measurement-quality indicators are actually a by-product of the virtual point transformation. Two different measurement-quality indicators can be calculated, i.e., the sensor consistency and the impact consistency [2]. In addition, an error indicator based on the expected reciprocity for the FRF of the VP was also proposed (see later). The presented expansion of the VPT does not affect the formulation of the quality indicators; therefore, sensor and impact consistency can be calculated without any modification.

4. Numerical case study

The proposed expansion of the virtual point transformation is demonstrated on a simple beam-like structure. Two virtual points are set in the center of a hole on each side of the structure, as shown in Fig. 6a. The dynamic response of the structure is obtained from a finite-element analysis, proposed free-free boundary condition (Fig. 6b). The geometry and material properties of the analyzed structure are presented in Table 1. For each virtual point, displacement and rotational FRFs were synthesised at 3 separate

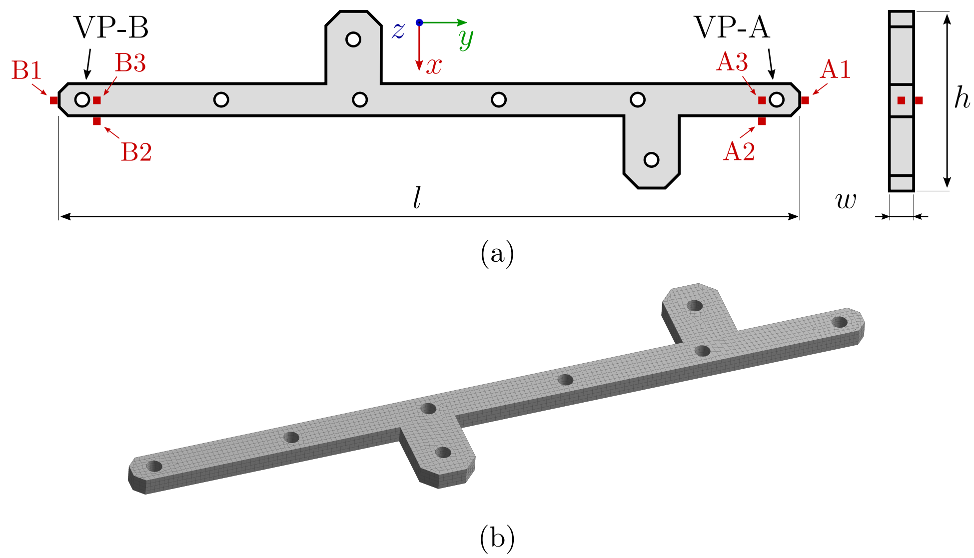

Figure 6: Beam-like structure with 2 virtual points and three sensor locations (red) for each virtual point: a) schematic representation; b) FEM model.

Table 1: Beam-like structure's geometrical and material properties.

Parameter	Unit	Value
l	mm	800
h	mm	190
w	mm	20
ρ	kg/m^3	7933
E	GPa	210

locations through inversion of dynamic stiffness with a constant damping ratio[3] of $\xi = 5\%$ (see Fig. 6a). Twelve different impact locations per virtual point were simulated. The impact locations in direct line of sight are depicted with red arrows and others with grey arrows in Fig. 9a. Overall, 864 FRFs were generated ($\mathbf{Y}_{\text{sim}} \in \mathbb{C}^{36\times24}$) from the numerical model, stretching a frequency bandwidth from zero to 3 kHz. The rotational and translational FRFs were averaged from the nodal displacements obtained from nodes on the surface over an 8×8 mm area, to replicate the experimental measurement

[3]Applied constant damping ratio was defined using the ANSYS APDL command DMPSTR.

of the FRF. Uncertainties associated with real measurements (i.e. measurement noise, sensor and impact location or orientation error) were excluded from the numerical simulation; however, small error in the transformation should be expected due to the averaging over an area and the deformation of the interface. Additionally, driving- and transfer-point VP FRFs were computed using the multipoint constraint elements MPC184 for reference.[4]

The analysed beam-like structure is symmetric over the x-y plane (see Fig. 6a). Thus, some of the directions are inherently uncoupled (such as q_x-q_z, q_y-q_z, q_z-θ_z, etc.). The corresponding off-diagonal terms in the FRF matrix should therefore be very small compared to driving point transfer functions. If the FE model would be fully symmetric the FRFs between uncoupled directions would be zero for DoFs on the neutral axis (here the axis of symmetry) and be very small for DoFs on θ and lower surfaces since the thickness of the structure is small.

4.1. Virtual point transformation

The virtual point transformation was applied to transform the synthesised FRF matrix to a virtual point FRF matrix. Two different transformations were considered. The first one was the standard VPT with three tri-axial translation sensors. The second one was the expanded VPT with two tri-axial translation sensors and one tri-axial rotational sensor per virtual point (sensor A2 and B2 depicted in Fig. 6a). The displacement and force weighting matrices were chosen to be the identity matrix and the rotational weighting matrix was calculated by Eq. (19) for consistent comparison between the two transformations. The coherence criterion [24] was used to assess the overall reciprocity of VP FRF matrix and with that the quality of both transformations:

$$\chi_{ij} = \mathrm{coh}(\mathrm{Y}_{ij}, \mathrm{Y}_{ji}) = \frac{(\mathrm{Y}_{ij} + \mathrm{Y}_{ji})(\overline{\mathrm{Y}}_{ij} + \overline{\mathrm{Y}}_{ji})}{2(\overline{\mathrm{Y}}_{ij}\,\mathrm{Y}_{ij} + \overline{\mathrm{Y}}_{ji}\,\mathrm{Y}_{ji})}. \tag{21}$$

The norm of the residuals in translations and rotations could also be used as a quality indicator; however, low norm of the residuals and with that high

[4]VP DoF were averaged from the nodal displacements near each VP and applied loads were distributed over the same nodes. Constraint equations created with the MPC184 elements can be regarded similar to those created with the RBE3 elements. No artificial stiffening is introduced to the model by using this type of formulation.

sensor and impact consistency does not necessarily mean a truthful VP FRF matrix [2].

Figure 7 shows the frequency-averaged reciprocity of the transformed VP admittance matrix for the two transformations. The uncoupled directions are shown semitransparent. The average reciprocity of the standard VPT over the whole frequency bandwidth is 75%, while the expanded VPT with rotations has an average reciprocity of 83%. The largest deviations in the reciprocity are observed in the inherently uncoupled directions (the symmetry over the x-y plane). An excitation in the x or y direction leads to a negligible response in the z direction; therefore, even a small uncertainty in the excitation or the response can lead to a large reciprocity error.

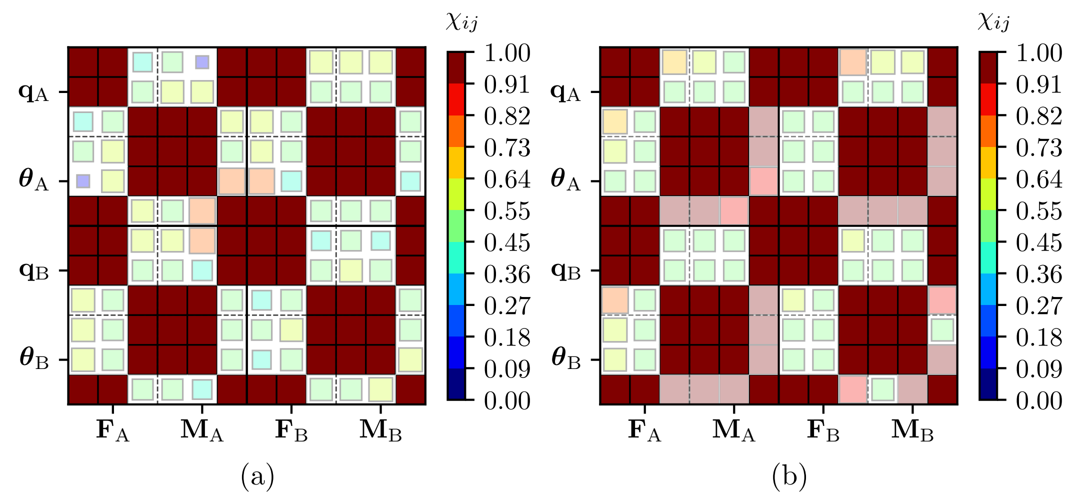

Figure 7: Frequency-averaged reciprocity of the transformed virtual point FRF matrix: a) standard VPT; b) expanded VPT with rotations.

The transformed FRFs for the two cases of transformation and numerically obtained reference VP FRFs obtained from the numerical model are depicted in Fig. 8. It is clear that in most directions both transformations are in good agreement with the reference FRF, as seen in Figures 8a, 8b and 8c. But for the inherently uncoupled direction as an example Fig. 8d both transformation are erroneous. For that reason the comparison of both transformations will not be performed on the uncoupled directions. The results in those directions will be shown semitransparent.

From Fig. 8d, we also observe that, for the higher frequency range, the FRFs obtained by the the VPT and from the MPC184 averaging at the connection differ. This is indicates that at higher frequencies it is not enough to consider the interface as behaving rigidly: considering the averaged displacements in the MPC184 is no longer meaningful and, for the VPT, additional interface deformation modes should be considered (as was for instance proposed in [5])

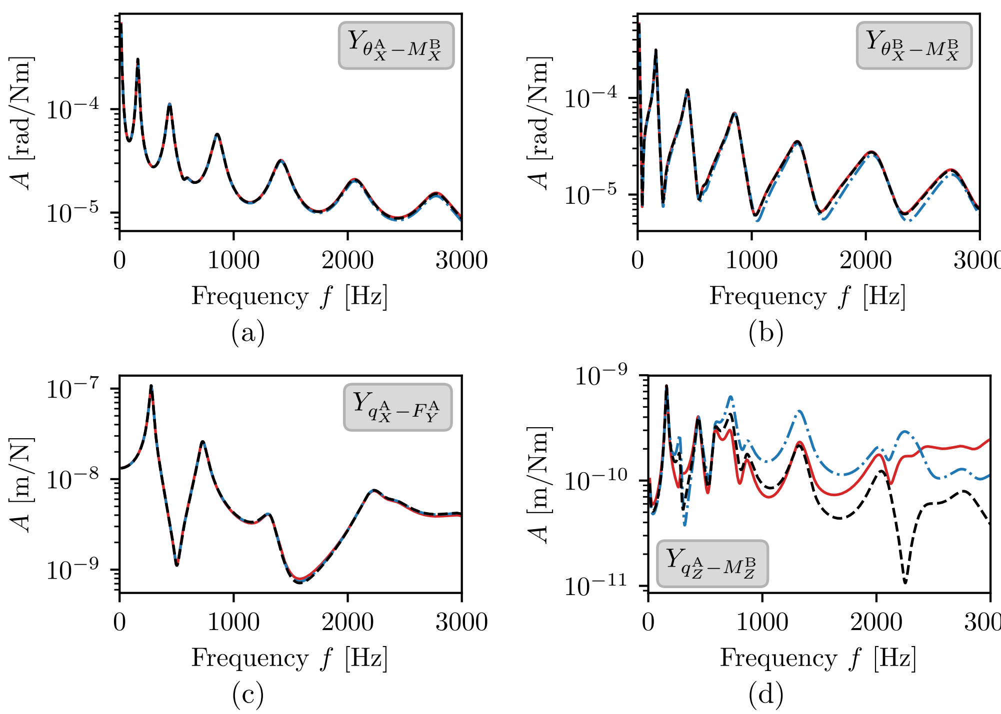

Figure 8: Comparison between expanded VPT with rotations, standard VPT and numerically obtained FRFs for VP: a) $\mathrm{Y}_{\theta_X^A\text{-}M_X^B}$; b) $\mathrm{Y}_{\theta_X^B\text{-}M_X^B}$; c) $\mathrm{Y}_{q_X^A\text{-}F_Y^A}$; d) $\mathrm{Y}_{q_Z^A\text{-}M_Z^B}$. Expanded VPT with rotations (—), standard VPT (-·-), reference FRF (- - -) (simulated measurements without any noise or location error).

4.2. Global sensitivity analysis

The overall quality of the virtual point transformation is primarily dependent on the sensor and impact positioning. Even a small uncertainty in the sensor and impact orientation or location can lead to an erroneous transformation. The effect of a small deviation in the direction of the impacts on the quality of the VPT has already been considered in [2]; therefore, that effect will be omitted in the analysis (i.e., the impact location and orientation are correct).

Firstly, small deviations in the sensor location, as depicted in Fig. 9, are considered and its effect is analyzed in terms of the overall quality of the

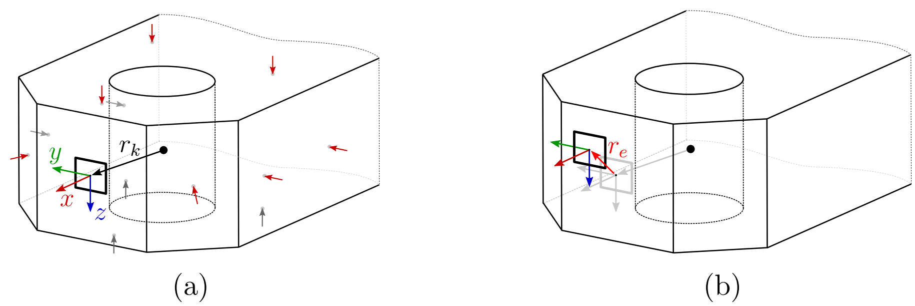

Figure 9: Virtual point location with sensor and impact locations: a) correct sensor position; b) small deviation in sensor position.

transformation. The evaluation model is equal to:

$$\chi_{ij}(\mathbf{r}_e^{1^{\mathrm{A}}}, \mathbf{r}_e^{2^{\mathrm{A}}}, \mathbf{r}_e^{3^{\mathrm{A}}}, \mathbf{r}_e^{1^{\mathrm{B}}}, \mathbf{r}_e^{2^{\mathrm{B}}}, \mathbf{r}_e^{3^{\mathrm{B}}}) = \mathrm{coh}(\mathrm{Y}_{ij}, \mathrm{Y}_{ji}) \qquad \mathrm{Y}_{ij}, \mathrm{Y}_{ji} \in \mathbf{Y}_{\mathrm{qm}}, \tag{22}$$

where χ_{ij} is a scalar value of the averaged coherence (Eq. (21)) over the whole frequency bandwidth and $\mathbf{r}_e^* = [r_x^*, r_y^*, r_z^*]$ is a vector of deviations in each sensor location.

Secondly, the effect of the deviation in the sensors' sensitivity is analysed. The evaluation model for the second case is equal to:

$$\chi_{ij}\big(\mathbf{s}_e^{1^{\mathrm{A}}}, \mathbf{s}_e^{2^{\mathrm{A}}}, \mathbf{s}_e^{3^{\mathrm{A}}}, \mathbf{s}_e^{1^{\mathrm{B}}}, \mathbf{s}_e^{2^{\mathrm{B}}}, \mathbf{s}_e^{3^{\mathrm{B}}}\big) = \mathrm{coh}(\mathrm{Y}_{ij}, \mathrm{Y}_{ji}) \qquad \mathrm{Y}_{ij}, \mathrm{Y}_{ji} \in \mathbf{Y}_{\mathrm{qm}}, \tag{23}$$

where $\mathbf{s}_e^* = [s_x^*, s_y^*, s_z^*]$ is the vector of the sensitivity deviations for each sensor. The locations of the sensors were assumed to be correct in this case.

4.2.1. Sobol's sensitivity analysis

There are many ways of evaluating the global sensitivity. Here, Sobol's sensitivity analysis[5] is used for reasons of its robustness and widespread usage. The method was originally developed by Sobol [35] in 2001 and then further improved by Saltelli et al. [36, 37]. The first-order Sobol's sensitivity index of each input parameter is calculated as:

$$S_1^{\chi_{ij}} = \frac{\mathbb{V}_{r_i}\big(\mathbb{E}_{r_{\sim i}}[\chi_{ij}|r_i]\big)}{\mathbb{V}(\chi_{ij})}, \tag{24}$$

[5]The method of global sensitivity indexes developed by Sobol is based on ANOVA decomposition, for more details see Appendix A.

where $\mathbb{V}(*)$ is the variance operator, $\mathbb{E}[*]$ is the expectation operator, r_i is the ith input parameter and $r_{\sim i}$ is a set of all the parameters except the r_i. The first-order index measures the main effect of the parameter r_i alone. The total effect index measures the effect of the parameter r_i, including all the higher-order interactions with other input parameters, and is defined as:

$$S_T^{\chi_{ij}} = 1 - \frac{\mathbb{V}_{r_{\sim i}}\big(\mathbb{E}_{r_i}[\chi_{ij}|r_{\sim i}]\big)}{\mathbb{V}(\chi_{ij})}. \tag{25}$$

The workflow of the global sensitivity analysis for the two evaluation models (Eq. (22) and (23)) is depicted in Fig. 10. Both the aformentioned transformations (standard and expanded) were analysed and compared with each other.

Firstly, the uncertainty in the sensor location was analysed (Fig. 10a). The location of each sensor was deviated inside a 5 mm interval according to the Saltelli sample scheme. For each iteration a virtual point transformation was performed and the coherence criterion (Eq. (21)) was calculated between the reference FRF and the transformed FRF. The reference FRF is calculated with the assumed correct location of the sensors.

Secondly, the uncertainty in the sensor sensitivity was analysed in a similar way (Fig. 10b). The sensitivity of each sensor axis was deviated inside a 5% interval according to the Saltelli sample scheme and the coherence criterion was calculated for each iteration.

4.2.2. Effect of the deviation in sensor location

Determining the correct locations for the sensors on large structures can be demanding and small uncertainties in the sensor placement are not uncommon. Figure 11 shows the FRFs $\mathrm{Y}_{\theta_X^{\mathrm{A}}\text{-}M_X^{\mathrm{B}}}$ and $\mathrm{Y}_{\theta_X^{\mathrm{B}}\text{-}M_X^{\mathrm{B}}}$ with small random deviations $r_e^* = 5$mm in the location of the sensors. It was shown that the FRFs are very similar for the standard and expanded VPT with rotations if the correct positions of the sensors are assumed (Fig. 8). However, even a small random deviation in the location of the sensors have a considerable effect on the standard VPT and negligible effect on the expanded VPT with rotations.

The first-order and total-order Sobol sensitivity indexes for the influence of sensor-location deviations on the FRF $\mathrm{Y}_{\theta_X^{\mathrm{B}}\text{-}M_X^{\mathrm{B}}}$ are shown in Fig. 12. If the sensor is misplaced in one direction (e.g. $\mathrm{r}_e^{2^{B_y}}$ which has negligible first-order sensitivity index), then the misplacement in that particular direction has

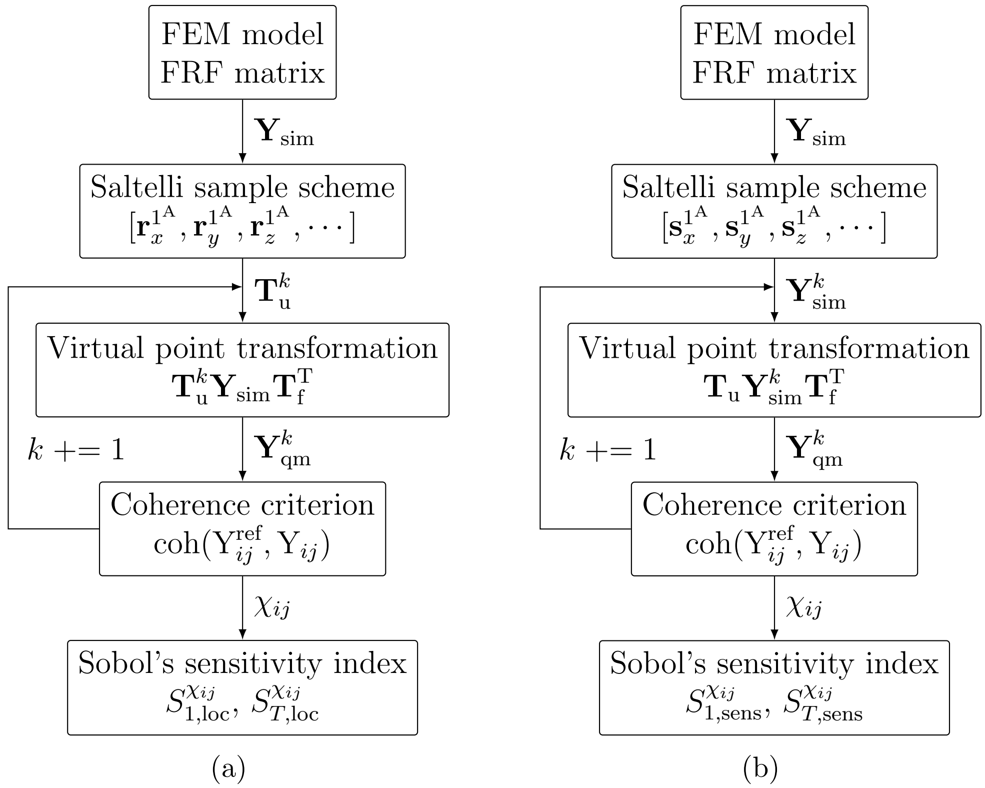

Figure 10: Workflow of the global sensitivity calculation: a) deviation in the sensor location; b) deviation in the sensor sensitivity.

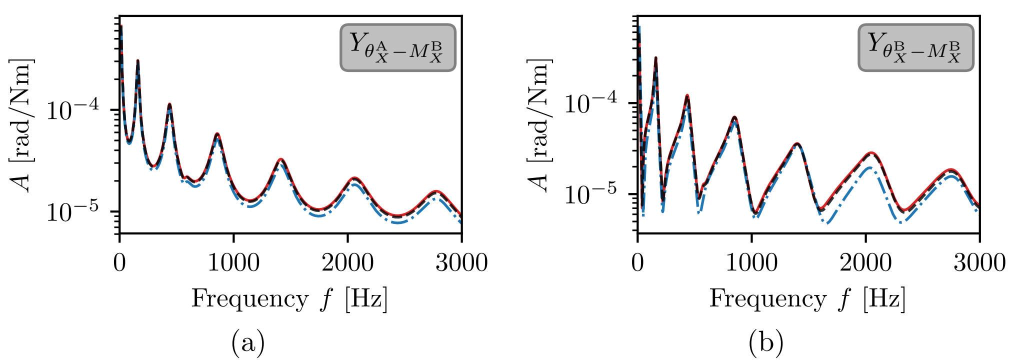

Figure 11: Effect of small random deviations ($r_e^* = 5$mm) in the sensors location on the FRF: a) $\text{Y}_{\theta_X^{\text{A}}\text{-}M_X^{\text{B}}}$; b) $\text{Y}_{\theta_X^{\text{B}}\text{-}M_X^{\text{B}}}$. Expanded VPT with rotations (▬▬), standard VPT (-·-·), reference FRF (- - -).

an effect on the observed FRFs in combination with misplacement in other directions. Additionally, this also implies that the misplacement in single direction will never effect only the observed FRFs but also FRFs in other directions. Therefore, a clear advantage of the expanded VPT with rotations is seen, since the deviations in the position of the rotational sensor has no effect on the transformed FRF (the position of the rotational sensor is only used to define a proper norm of the residuals see Eq. (19)).

Figure 13 shows the averaged total-order Sobol sensitivity indexes for the whole VP FRF matrix. A deviation of the sensor location is less impactful for the expanded VPT with rotations than for the standard VPT.

A deviation in the sensor location can also be detected by the overall sensor consistency [2]. However, a small deviation in sensor location or sensor sensitivity leads to the same poor sensor consistency over the whole frequency range, therefore it is difficult to distinguish between these two effects.

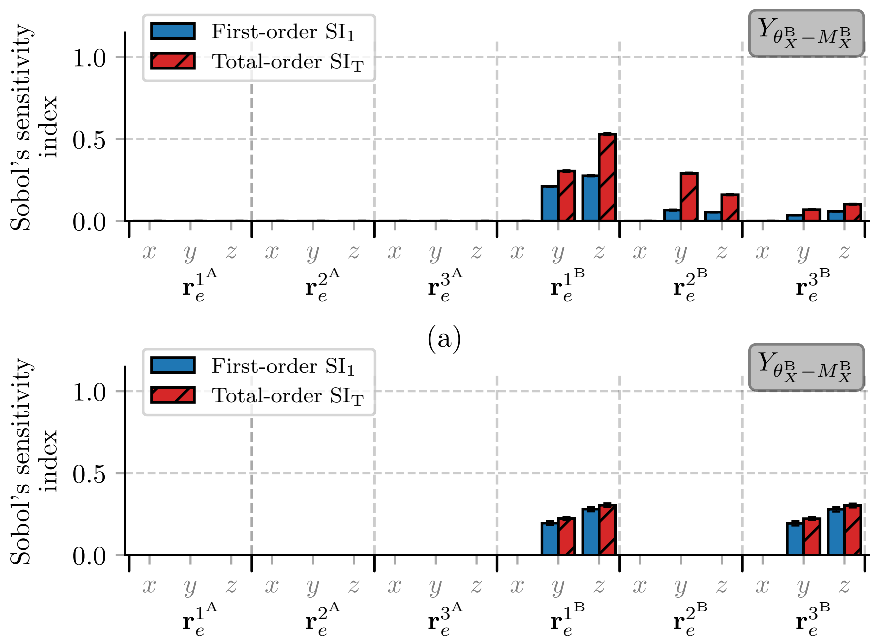

Figure 12: Sobol-sensitivity index for deviations in the sensor location for FRF $\mathrm{Y}_{\theta_X^\mathrm{B}\text{-}M_X^\mathrm{B}}$: a) standard VPT; b) expanded VPT with rotations.

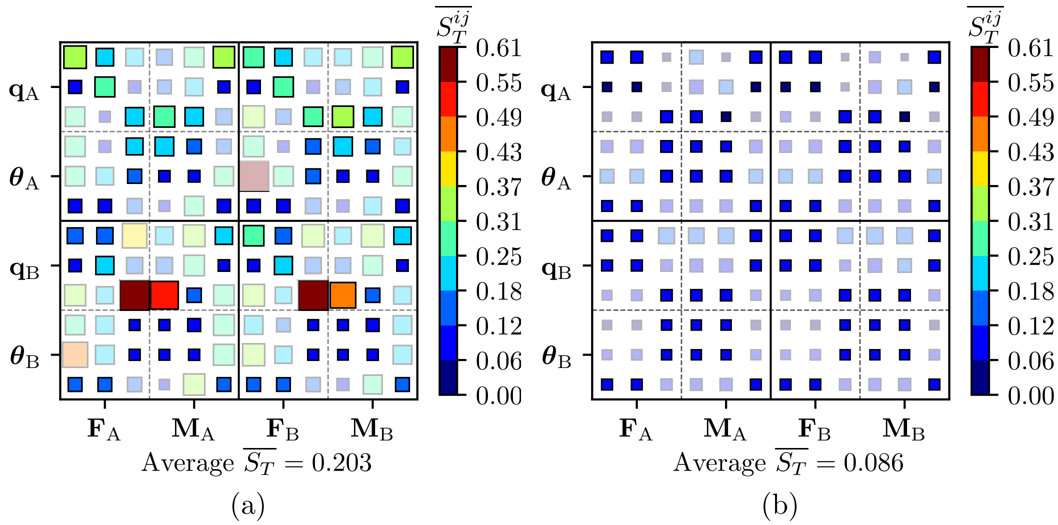

Figure 13: Averaged total-order Sobol-sensitivity index of the coherence criterion for deviations in the sensor location: a) standard VPT; b) expanded VPT with rotations.

4.2.3. Effect of the sensor measurement sensitivity deviation

The sensor measurement sensitivity should be determined annually with a proper calibration procedure [38]. Measurement sensitivity is always determined with an appropriate confidence interval. The size of the interval is determined by the sensor quality, as well as the calibration procedure. For that reason small deviations in the sensor measurement sensitivity are always present. Figure 14 shows the effect of small random deviations $s_e^* = 2\%$ in measurement sensitivity of the sensors on the FRFs $\mathrm{Y}_{\theta_X^\mathrm{A}\text{-}M_X^\mathrm{B}}$ and $\mathrm{Y}_{\theta_X^\mathrm{B}\text{-}M_X^\mathrm{B}}$ for both transformations. It is evident that the measurement sensitivity mismatch has a substantial effect on the standard VPT and practically negligible effect on the expanded VPT with rotations.

The first-order and total-order Sobol-sensitivity indexes for how small deviations in the measurement sensitivity effect the FRF $\mathrm{Y}_{\theta_X^\mathrm{B}\text{-}M_X^\mathrm{B}}$ are shown in Fig. 15. A similar conclusion can be drawn as before for deviations in the sensor placement. The standard VPT is more susceptible to small deviations in the sensor measurement sensitivity. In Fig. 16 the averaged total-order Sobol-sensitivity indexes for the whole VP FRF matrix are shown. It is evident that the expanded VPT with rotations is less prone to uncertainties in the sensor measurement sensitivity.

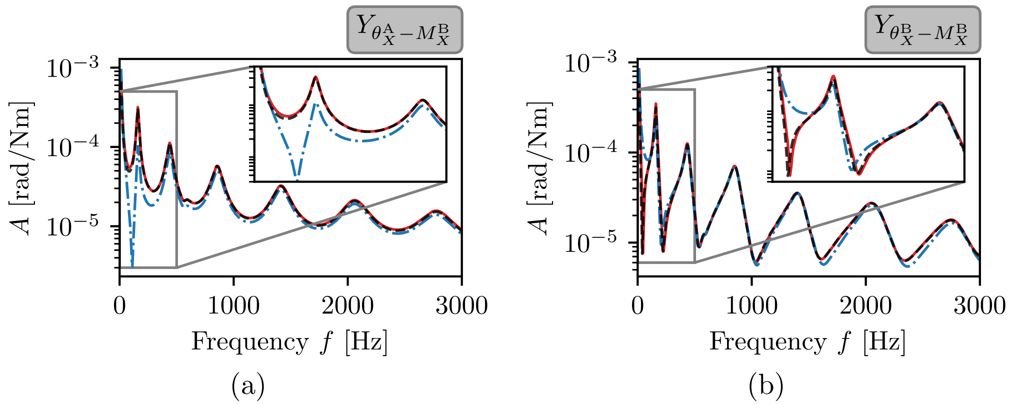

Figure 14: Effect of small random deviations ($s_e^* = 2\%$) of the sensors measurement sensitivity on the FRF: a) $\mathrm{Y}_{\theta_X^A\text{-}M_X^B}$; b) $\mathrm{Y}_{\theta_X^B\text{-}M_X^B}$. Expanded VPT with rotations (—), standard VPT (-·-), reference FRF (- - -).

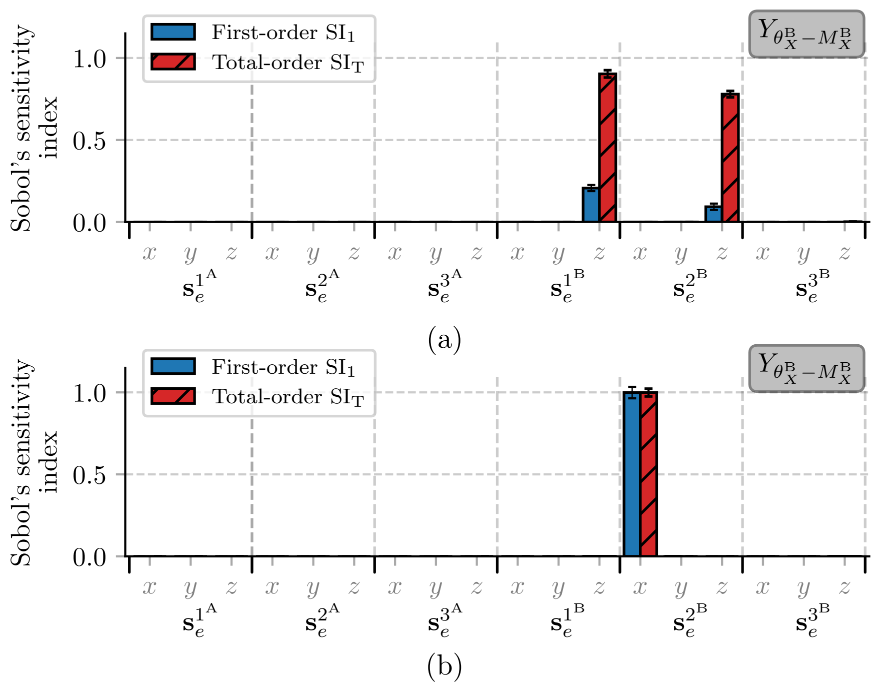

Figure 15: Sobol-sensitivity index for deviations in the sensor measurement sensitivity for the FRF $\mathrm{Y}_{\theta_X^B\text{-}M_X^B}$: a) standard VPT; b) expanded VPT with rotations.

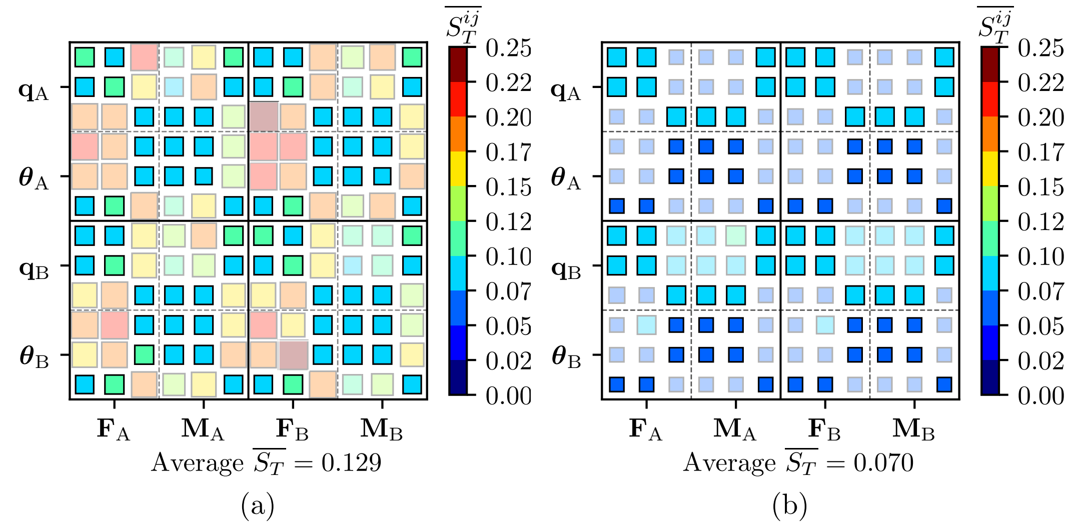

Figure 16: Averaged total-order Sobol-sensitivity index of the coherence criterion for deviations in the sensor measurement sensitivity: a) standard VPT; b) expanded VPT with rotations.

5. Experimental case study

This section demonstrates the practical applicability of the proposed expansion of the virtual point transformation. Both transformations, standard and expanded, were performed on two steel beams of different length in an approximately free-free boundary conditions. First a large beam with dimensions of $12 \times 40 \times 600$ mm was analysed (Fig. 17b), secondly, a small beam with dimensions $12 \times 40 \times 300$ mm (Fig. 17a). Only two degrees of freedom for each VP were considered (translational in the x direction and rotational around the z axis). The FRFs of the small beam obtained from standard and expanded transformations were coupled and compared with the reference FRFs obtained from both transformations on the large beam.

5.1. Measurement

The two virtual points L and R are set on each side of the two beams. Three Dytran 3097A2T single-axis accelerometers were attached near each VP, together with a Kistler 8840 rotational accelerometer (schematic representation of locations depicted in Fig. 18). Six different impact locations per VP were chosen and a PCB 086C03 modal hammer with an aluminium tip was used to excite the beams at each location. The FRF and coherence

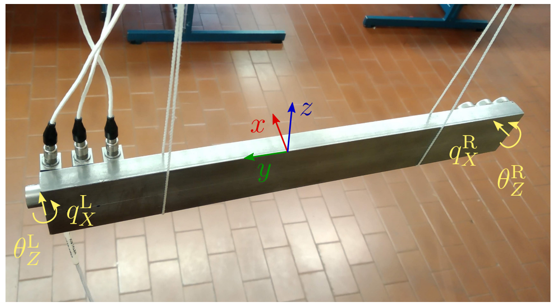

(a)

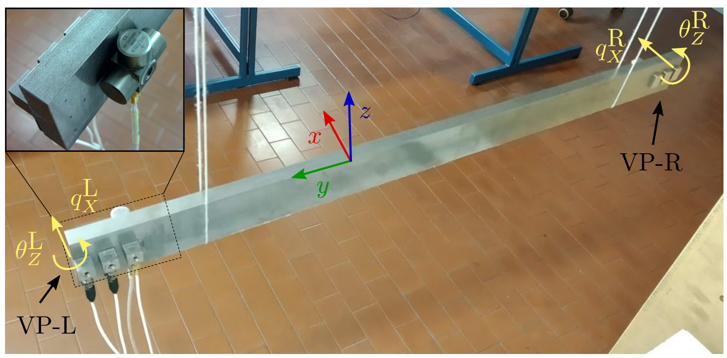

(b)

Figure 17: Experimental setup: a) small beam $12 \times 40 \times 300$ mm; b) large beam $12 \times 40 \times 600$ mm.

functions were obtained in the frequency range up to 2000 Hz with a 1 Hz spacing using the H_1 estimator. The frequency range is defined by a rotational accelerometer, since it is calibrated between 1 and 2000 Hz. However, relatively good agreement between the measured rotational response and the numerical reference was obtained in [11, 27] within the 3 kHz frequency range. Altogether, 96 FRFs were measured ($\mathbf{Y}_{\text{exp}} \in \mathbb{C}^{8\times 12}$) for both beams. With that, a sufficient over-determination for the transformations was obtained as only two degrees of freedom per VP were considered.

5.2. *Virtual point transformation results*

Two different displacement transformation matrices for the standard $\mathbf{T}_{\mathrm{u}}^{\mathrm{Std.}}$ and expanded $\mathbf{T}_{\mathrm{u},\theta}^{\mathrm{Exp.}}$ VPT were calculated for each beam. For the standard VPT only the three translational accelerometers were used and for the expanded VPT two translational accelerometers (the two near the VP), to-

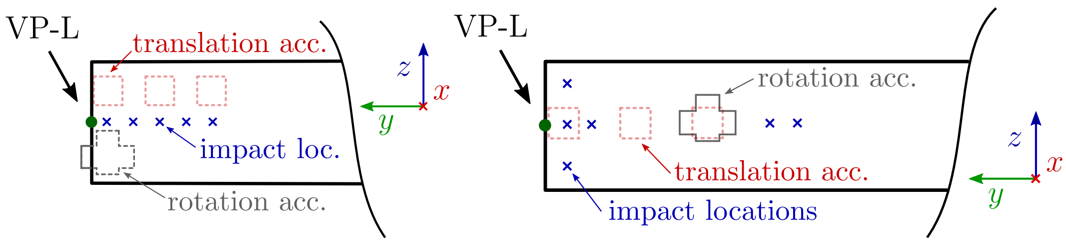

(a) (b)

Figure 18: Schematic representation of impact and sensor locations around the virtual point L: a) small beam; b) large beam.

gether with a rotational accelerometer. The force transformation matrix $\mathbf{T}_\mathrm{f}$ is the same for both transformations and was calculated based on the impact locations. The force and displacement weighting matrices were chosen to be an identity matrix and the rotational weighting matrix was calculated by Eq. (19) to objectively compare the two transformations. After applying both transformations, two 4×4 virtual point FRF matrices were obtained. The reciprocity of each transformation was assessed with the coherence criterion (Eq. (21)).

5.2.1. VPT on the large beam

Figure 19 shows the frequency-averaged reciprocity for both transformations. Only a small difference between each transformation can be observed, where the expanded VPT slightly outperforms the standard VPT. The total reciprocity averaged over all directions is around 98% for both transformations.

However, when looking at the reciprocal FRFs for each transformation the main advantage of the expanded VPT can be seen. In Fig. 20 the FRF $\mathrm{Y}_{q_X^\mathrm{R}\text{-}M_Z^\mathrm{R}}$ and their reciprocal $\mathrm{Y}_{\theta_Z^\mathrm{R}\text{-}F_X^\mathrm{R}}$ is shown. We can see a good agreement between the FRFs, except for around the anti-resonance region, where erroneous results are obtained from the standard VPT. The poorly defined anti-resonance is mostly due to small deviations in the sensor and impact positions, which are always present. In Fig. 21 a similar observation can be made for the transformations on the driving point FRFs $\mathrm{Y}_{\theta_Z^\mathrm{L}\text{-}M_Z^\mathrm{L}}$ and $\mathrm{Y}_{\theta_X^\mathrm{R}\text{-}M_Z^\mathrm{R}}$.

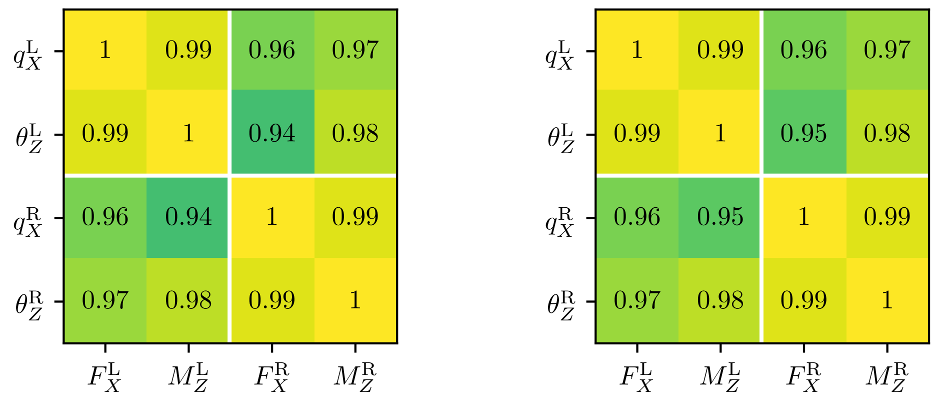

(a) (b)

Figure 19: Comparison of the coherence values between the reciprocal virtual point FRFs for both transformations on the large beam: a) standard VPT; b) expanded VPT.

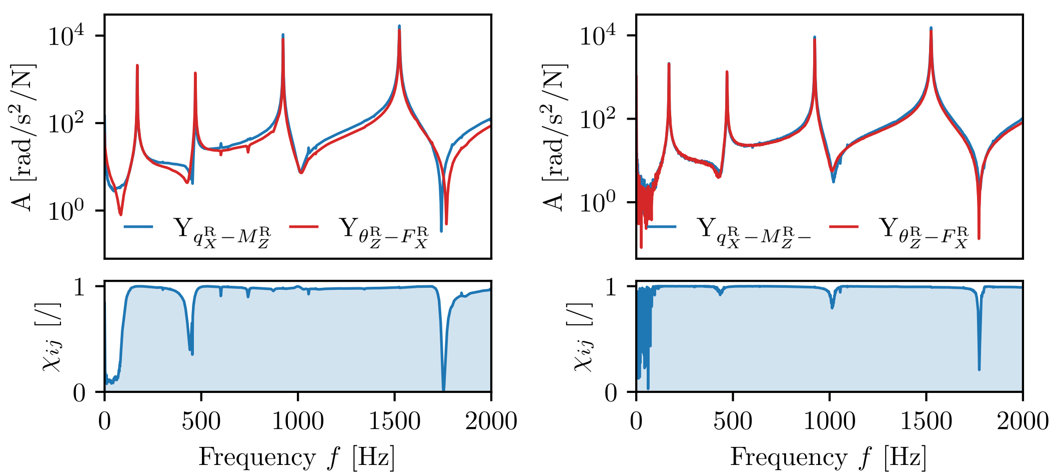

(a) (b)

Figure 20: Virtual point FRF $\mathrm{Y}_{q_X^{\mathrm{R}}\text{-}M_Z^{\mathrm{R}}}$ and their reciprocal $\mathrm{Y}_{\theta_Z^{\mathrm{R}}\text{-}F_X^{\mathrm{R}}}$ for both VP transformations on the large beam: a) standard VPT; b) expanded VPT.

5.2.2. VPT on the small beam

A simmilar comparison between the two transformations can be observed even on the small beam. In Fig. 22 the frequency-averaged reciprocity for both transformations is shown. The expanded VPT is slightly outperforms the standard VPT. The total reciprocity averaged over all directions is also

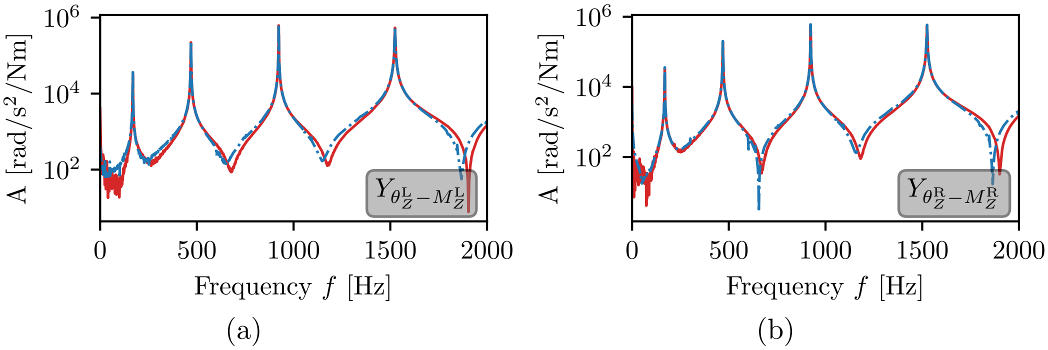

Figure 21: Driving point FRFs of virtual point for both transformations on the large beam: a) FRF $\mathrm{Y}_{\theta^{\mathrm{L}}_Z\text{-}M^{\mathrm{L}}_Z}$; b) FRF $\mathrm{Y}_{\theta^{\mathrm{R}}_X\text{-}M^{\mathrm{R}}_Z}$. Expanded VPT with rotations (——) and standard VPT (-·-).

around 98% for both transformations, as was on the large beam.

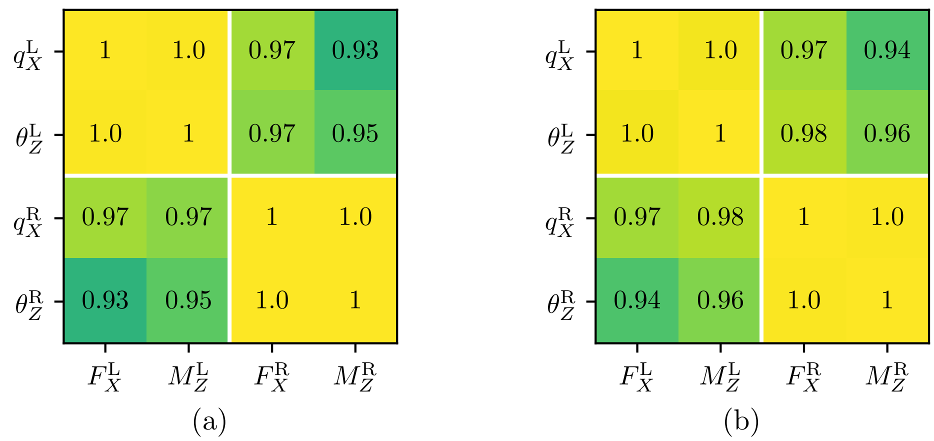

Figure 22: Comparison of the coherence values between the reciprocal virtual point FRFs for both transformations on the small beam: a) standard VPT; b) expanded VPT.

In Fig. 23 the reciprocal FRFs $\mathrm{Y}_{\theta^{\mathrm{L}}_Z\text{-}M^{\mathrm{R}}_Z}$ and $\mathrm{Y}_{\theta^{\mathrm{R}}_Z\text{-}M^{\mathrm{L}}_Z}$ are shown. The FRFs for both transformations are consistent with the expanded VPT being marginally more reciprocal. Only in the low frequency range a rather high levels of noise can be observed which is due to the noise present in the rotational FRFs obtained from rotational accelerometer [11, 27]. A frequency dependent weighting matrix could be defined using a coherence values of rotational FRFs to give lower weighting to the rotational accelerometer in the low-frequency range [26].

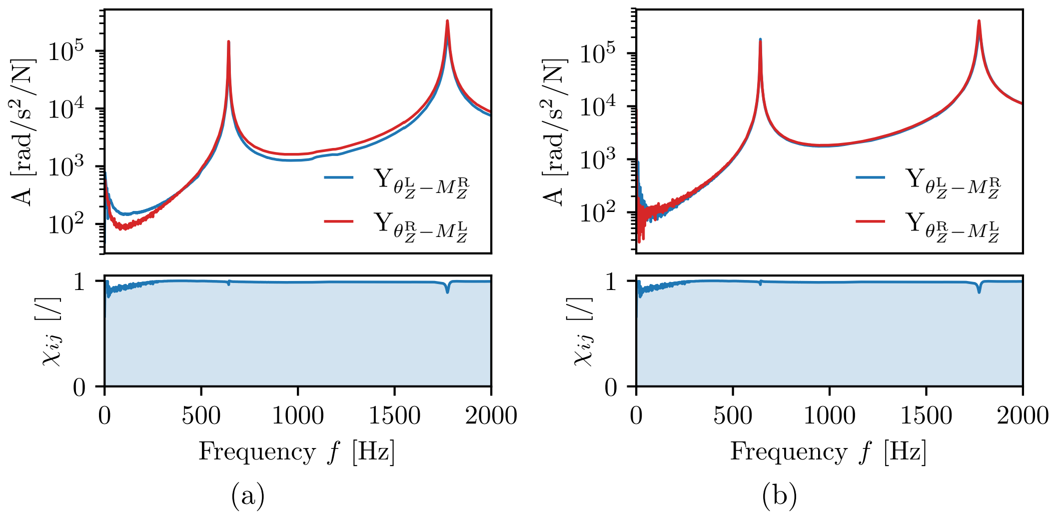

Figure 23: Virtual point FRF $\mathrm{Y}_{\theta_Z^{\mathrm{L}}\text{-}M_Z^{\mathrm{R}}}$ and their reciprocal $\mathrm{Y}_{\theta_Z^{\mathrm{R}}\text{-}M_Z^{\mathrm{L}}}$ for both VP transformations on the small beam: a) standard VPT; b) expanded VPT.

5.3. Substructuring results

Four different VP FRFs sets were evaluated to experimentally validate the expanded VPT. Two reference VP FRFs were obtained by performing standard and expanded VPT on the large beam as depicted in Fig. 24. Two coupled VP FRFs were obtained by coupling the two VP FRFs of the small beam using the LM FBS method (Eq. (4)) as depicted in Fig. 25.

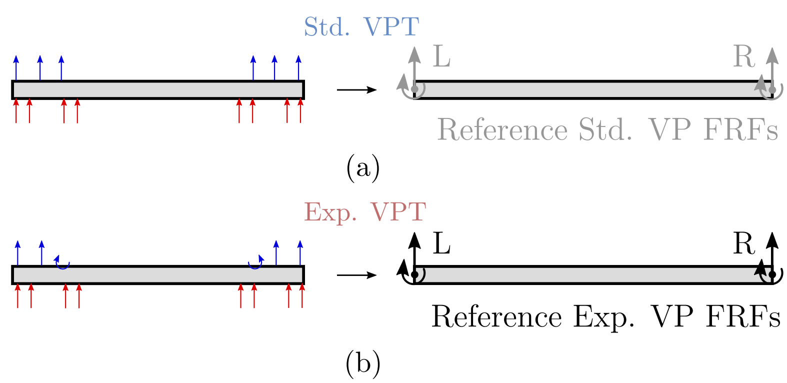

Figure 24: Schematic representation of workflow for calculating the reference VP FRFs from the large beam: a) standard VPT, b) expanded VPT with rotations.

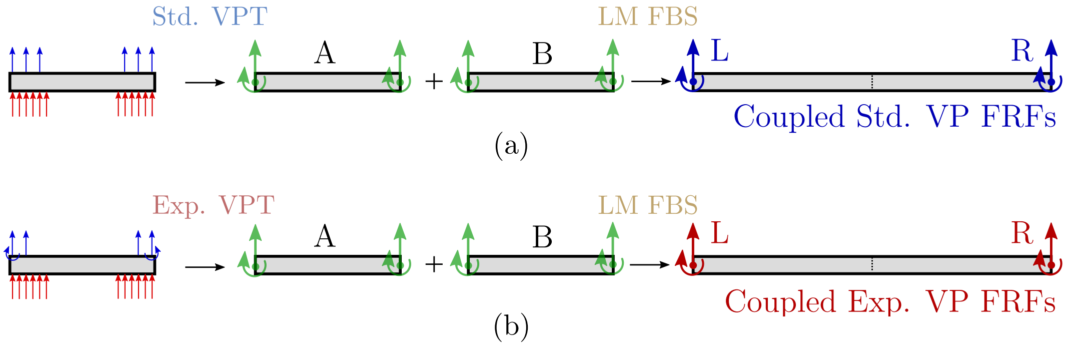

Figure 25: Schematic representation of workflow for calculating the coupled VP FRFs from the small beam: a) standard VPT, b) expanded VPT with rotations.

In Fig. 26 the reciprocal FRFs $\mathrm{Y}_{\theta_Z^{\mathrm{L}}\text{-}M_Z^{\mathrm{R}}}$ and $\mathrm{Y}_{\theta_Z^{\mathrm{R}}\text{-}M_Z^{\mathrm{L}}}$ obtained after coupling the two VPs of the small beam are shown. We can see that the coupled FRFs have a high reciprocity practically over the whole frequency range, except in the proximity of 700 Hz and 1750 Hz where two inconsistent peaks can be observed. The two spurious peaks appear at the position of the subsystem eigenfrequencies (i.e. small beam). These two spurious peaks are induced from small inconsistencies from the measurement. Even small inaccuracies in the vicinity of the eigenfrequencies of each subsystem can induce spurious peaks whenever lightly damped subsystem are coupled using the LM FBS method [39].

In Fig. 27a the VP FRF $\mathrm{Y}_{\theta_Z^{\mathrm{L}}\text{-}M_Z^{\mathrm{R}}}$ obtained from all four combinations is shown. The reference FRFs are similar for both transformations as was already shown. The location of eigenfrequencies is slightly shifted between the reference and coupled FRFs. This is probably due to the effect of different mass loading of the sensors during measurement of the FRFs on both beams, since there are no sensors placed around the interface on the long beam (see Fig. 17b). However, a slight improvement can be observed on the coupled VP using the expanded VPT considering the amplitude of the coupled FRF at the position of eigenfrequencies (see Fig. 27b). This could be related to more consistent VP FRFs obtained from the expanded VPT. A similar relations can be observed for the VP FRF $\mathrm{Y}_{\theta_Z^{\mathrm{R}}\text{-}M_Z^{\mathrm{R}}}$ shown in Fig. 28.

The use of a directly measured rotational response in the virtual point transformation can increase the reliability and validity of the whole transformation; however, the coupled FRFs from the standard VPT and expanded

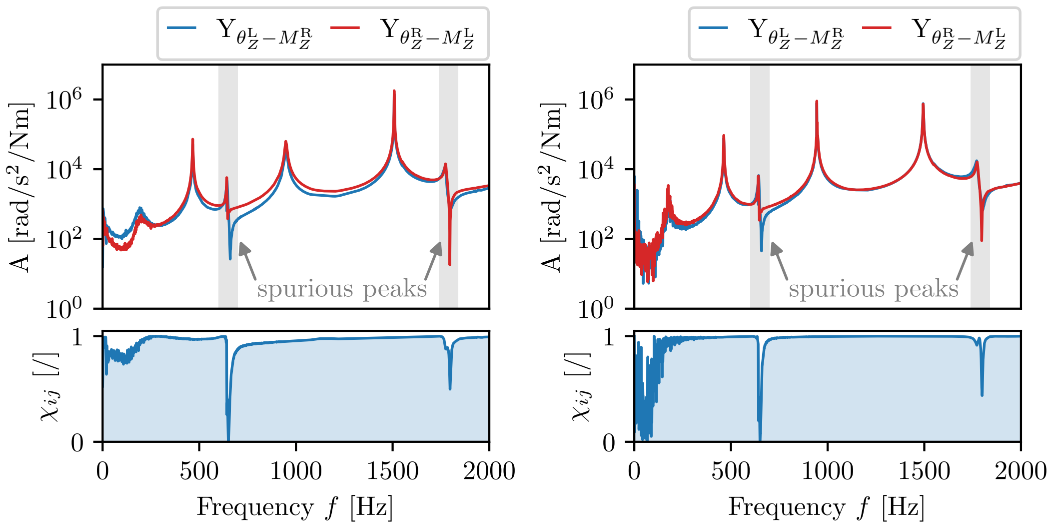

(a) (b)

Figure 26: Coupled virtual point FRF $Y_{\theta_Z^L\text{-}M_Z^R}$ and their reciprocal $Y_{\theta_Z^R\text{-}M_Z^L}$: a) standard VPT; b) expanded VPT.

are similar except for the amplitude at the position of eigenfrequencies. The expanded virtual point transformation does not remove spurious peaks from the assembled system located at the local eigenfrequencies of each subsystem.

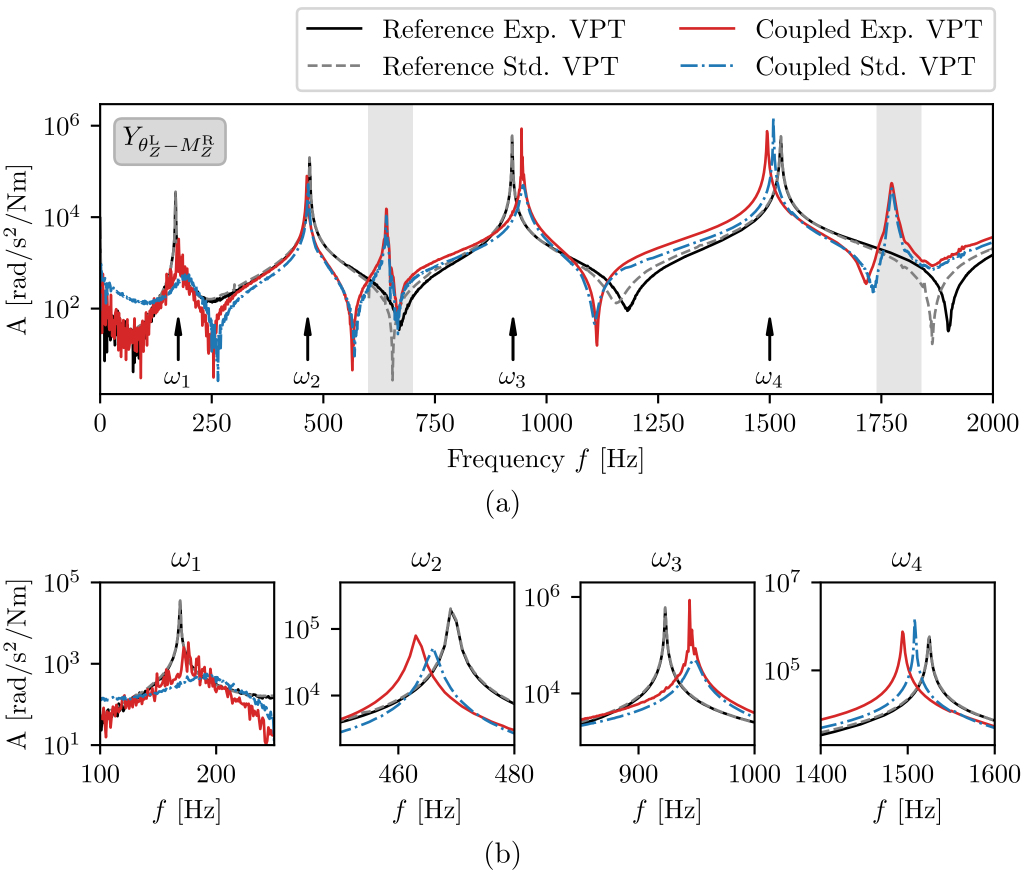

Figure 27: Comparison between coupled and reference VP FRF $\mathrm{Y}_{\theta_Z^{\mathrm{L}}\text{-}M_Z^{\mathrm{R}}}$ obtained from standard and expanded VPT: a) the whole frequency range b) zoomed-in region around each eigenfrequency.

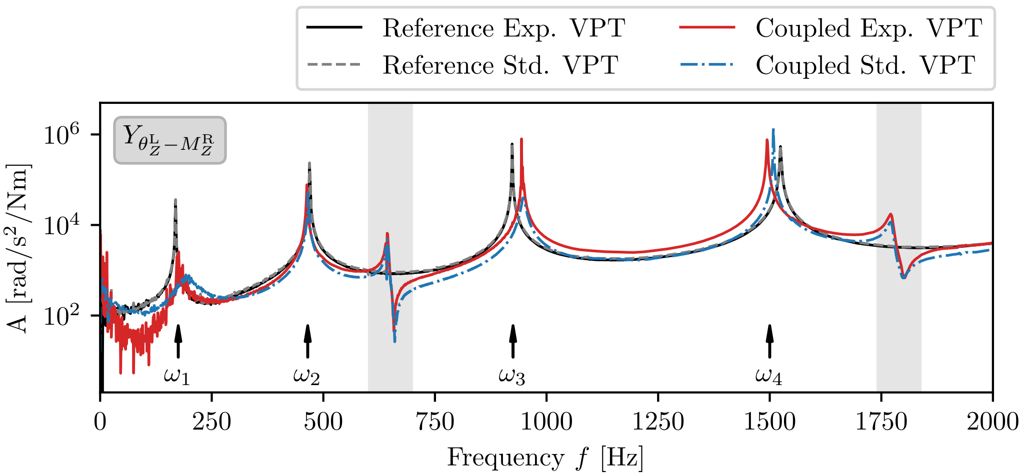

(a)

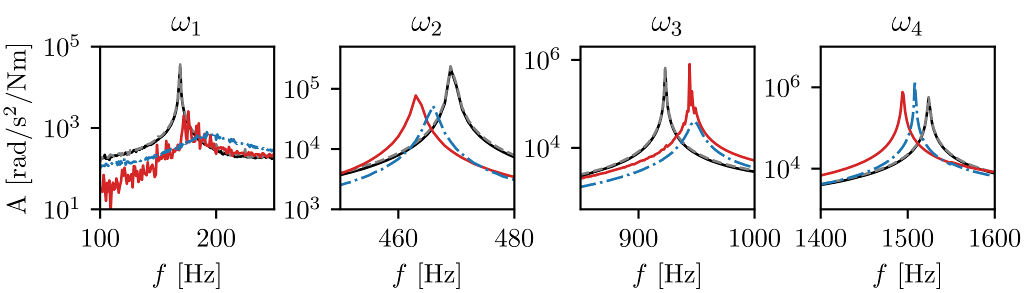

(b)

Figure 28: Comparison between coupled and reference VP FRF $Y_{\theta_Z^L\text{-}M_Z^R}$ obtained from standard and expanded VPT: a) the whole frequency range b) zoomed-in region around each eigenfrequency.

6. Conclusion

This paper presents an expansion of the standard virtual point transformation with directly measured rotational degrees of freedom. The expanded VPT enables the projection of measured rotation responses on the interface deformation modes. The applicability of the proposed expansion was demonstrated on a numerical case study, where standard and expanded VPTs were performed on a simple beam-like structure. A global sensitivity analysis was performed to gain an insight into how small inaccuracies in the sensor position or the sensor measurement sensitivity effect the overall quality of both transformations. The expanded VPT is less sensitive to small inaccuracies in comparison with the standard VPT. The expansion was experimentally validated on a beam structure where promising results can be obtained with the inclusion of a rotation response, especially within the anti-resonance regions of the VP FRFs. The inherent noise of the rotational accelerometer was shown to have an effect on the VP FRFs in the low-frequency range up to 300 Hz. The presented expansion of the VPT can decrease the uncertainties associated with the sensor position and sensitivity when performing application on real structures.

Appendix A. Sobol sensitivity analysis

The method of global sensitivity indexes developed by Sobol is based on the analysis of variance (ANOVA) decomposition [35]. Consider that the evaluation model is described by a square integrable function $f(\boldsymbol{x})$ defined in the unit hypercube $I^n = [0,1]^n$:

$$u = f(\boldsymbol{x}) = f(x_1, \ldots, x_n). \tag{A.1}$$

where u is a scalar output and $\boldsymbol{x}$ an input inside the unit hypercube. The first step to Sobol's method is the decomposition of the evaluation function in the following form:

$$u = f(x_1, \ldots, x_n) = f_0 + \sum_{i=1}^{n} f_i(x_i) + \sum_{i<j} f_{ij}(x_i, x_j) + \cdots + f_{1\ldots n}(x_1, \ldots, x_n), \tag{A.2}$$

where $f_0 = \int f(\boldsymbol{x})\mathrm{d}x$. The decomposition is unique if the integral of each term $f_{i_1 \ldots i_s}(x_{i_1}, \ldots, x_{i_s})$ over any independent variable is zero:

$$\int f_{i_1 \ldots i_s}(x_{i_1}, \ldots, x_{i_s})\mathrm{d}x_k = 0 \quad \text{for} \quad k = i_1, \ldots, i_s. \tag{A.3}$$

It follows that all the terms in (A.2) are mutually orthogonal and can be expressed as integrals of $f(\boldsymbol{x})$. As assumed, the function $f(\boldsymbol{x})$ is square integrable:

$$\begin{aligned} \underbrace{\int f^2(\boldsymbol{x})\mathrm{d}\boldsymbol{x} - f_0^2}_{D} = \sum_{i=1}^{n} \underbrace{\int f_i^2(x_i)\mathrm{d}x_i}_{D_i} + \sum_{i<j} \underbrace{\int f_{ij}^2(x_i, x_j)\mathrm{d}x_i\mathrm{d}x_j}_{D_{ij}} + \cdots + \\ + \underbrace{\int f_{1\ldots n}^2(x_1, \ldots, x_n)\mathrm{d}x_1 \cdots \mathrm{d}x_n}_{D_{12\ldots n}}, \end{aligned} \tag{A.4}$$

where D is the total variance and D_i, D_{ij} and $D_{12\ldots n}$ are partial variances. Dividing both sides of the equation (A.4) by the total variance D we obtain the definition of the global sensitivity indexes:

$$\sum_{i=1}^{n} \underbrace{\frac{D_i}{D}}_{S_i} + \sum_{i<j} \underbrace{\frac{D_{ij}}{D}}_{S_{ij}} + \cdots + \underbrace{\frac{D_{12\ldots n}}{D}}_{S_{12\ldots n}} = 1. \tag{A.5}$$

The most commonly used sensitivity indexes are the so-called first-order and total-order indexes. The first-order sensitivity index S_i defines the first-order effect of x_i on the model output and the total-order sensitivity index S_i^T the total effect, i.e., the first and all the higher-order effects of the factor x_i.

The main advantage of the Sobol sensitivity analysis is the computation algorithm that allows an estimation of the global sensitivity indexes using only the output values of $f(\boldsymbol{x})$. Monte Carlo sampling-based methods have been developed for first-order and interaction indexes by Sobol [35] and additionally for a total-order index by Saltelli [36].

References

[1] D. de Klerk, D. J. Rixen, S. N. Voormeeren, General Framework for Dynamic Substructuring: History, Review and Classification of Techniques, AIAA Journal 46 (5) (2008) 1169–1181.

[2] M. V. van der Seijs, Experimental Dynamic Substructuring: Analysis and design strategies for vehicle development, Ph.D. thesis, TU Delft (2016).

[3] D. de Klerk, How Bias Errors Affect Experimental Dynamic Substructuring, in: Proceedings of the 28th International Modal Analysis Conference, A Conference on Structural Dynamics (2011) 1101–1112.

[4] D. de Klerk, S. N. Voormeeren, Uncertainty Propagation in Experimental Dynamic Substructuring, in: Proceedings of the 26th International Modal Analysis Conference, A Conference on Structural Dynamics, (2008).

[5] E. A. Pasma, M. V. van der Seijs, S. W. B. Klaassen, M. W. van der Kooij, Frequency Based Substructuring with the Virtual Point Transformation, Flexible Interface Modes and a Transmission Simulator, in: Conference Proceedings of the Society for Experimental Mechanics Series 4 (2018) 205–213.

[6] B. Jetmundsen, R. L. Bielawa, W. G. Flannely, Generalized Frequency Domain Substructure Synthesis, Journal of the American Helicopter Society 33 (1) (1988) 55–64.

[7] W. Duncan, The admittance method for obtaining the natural frequencies of systems, The London, Edinburgh, and Dublin Philosophical Magazine and Journal of Science 32 (214) (1941) 401–409.

[8] R. Bishop, D. Johnson, The mechanics of vibration, Cambridge University Press, UK, (1960).

[9] P. Avitabile, J. O'Callahan, Frequency Response Function Expansion for Unmeasured Translation and Rotation Dofs for Impedance Modelling Applications, Mechanical Systems and Signal Processing 17 (4) (2003) 723–745.

[10] D. de Klerk, D. J. Rixen, J. de Jong, The Frequency Based Substructuring (FBS) Method reformulated according to the Dual Domain Decomposition Method, in: Proceedings of the 24th International Modal Analysis Conference, A Conference on Structural Dynamics, (2006).

[11] A. Drozg, G. Čepon, M. Boltežar, Full-degrees-of-freedom frequency based substructuring, Mechanical Systems and Signal Processing 127 (2018) 570–579.

[12] D. de Klerk, D. J. Rixen, S. N. Voormeeren, F. Pasteuning, Solving the RDoF Problem in Experimental Dynamic Substructuring, in: Proceedings of the 26th International Modal Analysis Conference, A Conference on Structural Dynamics, (2010).

[13] M. L. M. Duarte, D. J. Ewins, Some Insights into the Importance of Rotational Degrees-of-freedom and Residual Terms in Coupled Structure Analysis, in: Proceedings of the 13th International Modal Analysis Conference, A Conference on Structural Dynamics (1995) 164–170.

[14] J. O'Callahan, P. Avitabile, R. Riemer, System equivalent reduction expansion process, in: Proceedings of the 7th International Modal Analysis Conference, A Conference on Structural Dynamics, (1989).

[15] A. Williams, C. C. Chipman, P. Avitabile, Modal and frequency based substructuring using rotational DOF considerations, in: Proceedings of the 26th International Modal Analysis Conference, A Conference on Structural Dynamics, (2008).

[16] Y. Y. Kim, J. H. Kang, A New Experimental Method to Determine Rotational Modes from the Strain Measurement, in: Proceedings of SPIE - The International Society for Optical Engineering, Orlando, FL, Society for Experimental Mechanics (1997) 1415–1418.

[17] S. S. Sattinger, Method for Experimentally Determining Rotational Mobilities of Structures, Shock and Vibration Bulletin 50 (6) (1980) 55–64.

[18] S. Jianxin, C. M. Mak, Direct measurement of moment mobility and a moment excitation system, Applied Acoustics 63 (2) (2002) 139–151.

[19] T. A. N. Silva, N. M. M. Maia, Estimation of Rotational Frequency Response Functions, in: Proceedings of the 33rd IMAC, A Conference and Exposition on Structural Dynamics (2015) 35–48.

[20] J. E. Mottershead, M. G. Tehrani, D. Stancioiu, S. James, H. Shahverdi, Structural modification of a helicopter tailcone, Journal of Sound and Vibration 298 (1-2) (2006) 366–384.

[21] R. Mayes, Tutorial on Experimental Dynamic Substructuring using the Transmission Simulator Method, in: Proceedings of the 30th International Modal Analysis Conference, A Conference on Structural Dynamics 3 (2012) 1–9.

[22] R. L. Mayes, M. R. Ross, Advancements in hybrid dynamic models combining experimental and finite element substructures, Mechanical Systems and Signal Processing 31 (2012) 55–66.

[23] M. S. Allen, R. L. Mayes, E. J. Bergman, Experimental modal substructuring to couple and uncouple substructures with flexible fixtures and multi-point connections, Journal of Sound and Vibration 23 (329) (2010) 4891–4906.

[24] M. van der Seijs, D. van den Bosch, D. J. Rixen, D. de Klerk, An improved methodology for the virtual point transformation of measured frequency response functions in dynamic substructuring, in: 4th ECCOMAS Thematic Conference on Computational Methods in Structural Dynamics and Earthquake Engineering (COMPDYN). (2013) 4334–4347.

[25] D. de Klerk, D. J. Rixen, S. N. Voormeeren, F. Pasteuning, Solving the RDoF Problem in Experimental Dynamic Substructuring, in: Proceedings of the 26th International Modal Analysis Conference, A Conference on Structural Dynamics (2008).

[26] M. Häußler, D. J. Rixen, Optimal transformation of frequency response functions on interface deformation modes, in: Dynamics of Coupled Structures, Volume 4, Springer International Publishing, 2017, pp. 225–237.

[27] A. Drozg, J. Rogelj, G. Čepon, M. Boltežar, On the performance of direct piezoelectric rotational accelerometers in experimental structural dynamics, Measurement 98 (2018) 292–298.

[28] M. V. van der Seijs, D. de Klerk, D. J. Rixen, S. Rahimi, Validation of current state Frequency Based Substructuring Technology for the characterisation of Steering Gear Vehicle Interaction, in: Conference Proceedings of the Society for Experimental Mechanics Series 2 (2013) 253–266.

[29] D. de Klerk, Dynamic Response Characterization of Complex Systems through Operational Identification and Dynamic Substructuring - An application to gear noise propagation in the automotive industry, Ph.D. thesis, TU Delft (2009).

[30] D. J. Ewins, M. G. Sainsbury, Mobility Measurement for the Vibration Analysis of Connected Structures, The Shock and Vibration Bulletin 42 (1) (1972) 105–113.

[31] D. J. Ewins, Modal Testing: Theory and Practice, Research Studies Press Ltd., (1984).

[32] M. Dumont, N. Kinsley, Rotational Accelerometers and Their Usage in Investigating Shaker Head Rotations, in: Sensors and Instrumentation, Volume 5, Conference Proceedings of the Society for Experimental Mechanics Series, Springer, Cham (2015) 8592.

[33] ISO, ISO 16063-21:2003: Methods for the calibration of vibration and shock transducers – Part 21: Vibration calibration by comparison to a reference transducer, 2003.

[34] M. D. Insalaco, The Art of Fabricating Rotational Accelerometer, Sensors Magazine (2000).

[35] I. M. Sobol, Global sensitivity indices for nonlinear mathematical models and their Monte Carlo estimates, Mathematics and Computers in Simulation 55 (1-3) (2001) 271–280.

[36] A. Saltelli, Making best use of model evaluations to compute sensitivity indices, Computer Physics Communications 145 (2) (2002) 280–297.

[37] A. Saltelli, P. Annoni, I. Azzini, F. Campolongo, M. Ratto, S. Tarantola, Variance based sensitivity analysis of model output. Design and estimator for the total sensitivity index, Computer Physics Communications 181 (2) (2010) 259–270.

[38] ISO, ISO 7626-1:2011: Mechanical vibration and shock – Experimental determination of mechanical mobility – Part 1: Basic terms and definitions, and transducer specifications, 2011.

[39] D. J. Rixen, How Measurement Inaccuracies Induce Spurious Peaks in Frequency Based Substructuring, in: Proceedings of the XXVI International Modal Analysis Conference, Society for Experimental Mechanics, Orlando (2008).